Additive Manufacturing for Cost Efficient Production of Compact Ceramic Heat Exchangers and Recuperators

Final Report

Reporting Period Start: November 1, 2014
Reporting Period End: October 30, 2015

Principal Authors: Dr. Holly Shulman (PI)
Nicole Ross

November 2015
DE-FE0024066

Submitting Organization

Ceralink Inc.
105 Jordan Rd
Troy, NY 12180

United Technologies Research Center
411 Silver Lane
East Hartford, CT 06108

DISCLAIMER

Abstract

An additive manufacture technique known as laminated object manufacturing (LOM) was used to fabricate compact ceramic heat exchanger prototypes. LOM uses precision CO_2 laser cutting of ceramic green tapes, which are then precision stacked to build a 3D object with fine internal features. Modeling was used to develop prototype designs and predict the thermal response, stress, and efficiency in the ceramic heat exchangers. Build testing and materials analyses were used to provide feedback for the design selection. During this development process, laminated object manufacturing protocols were established. This included laser optimization, strategies for fine feature integrity, lamination fluid control, green handling, and firing profile. Three full size prototypes were fabricated using two different designs. One prototype was selected for performance testing. During testing, cross talk leakage prevented the application of a high pressure differential, however, the prototype was successful at withstanding the high temperature operating conditions (1300 °F). In addition, analysis showed that the bulk of the part did not have cracks or leakage issues. This led to the development of a module method for next generation LOM heat exchangers. A scale-up cost analysis showed that given a purpose built LOM system, these ceramic heat exchangers would be affordable for the applications.

Contents

Executive Summary

The goal of this program was to advance the technology of compact high temperature ceramic heat exchangers as a component for high efficiency advanced power generation systems. Several mature and emerging technologies were combined to develop a novel heat exchanger. The program targeted the creation of a prototype capable of operating up to 1500 °F (816 °C), high thermal cycle efficiency, and low weight to volume ratio.

The important accomplishments of this program include: **1)** successful development of laminated object manufacturing for complex internal channels in large monolithic ceramics; **2)** creation of design protocols through modeling and build testing; **3)** full size prototype fabrication; **4)** novel apparatus design and ceramic performance testing to 1300 °F; **5)** a strategy for using laminated object manufacturing to build full scale ceramic heat exchangers in a production setting.

Laminated object manufacturing (LOM) of ceramics had previously been explored for small thin parts, with typically fewer than 20 layers for applications such as microfluidic separation. This project advanced the state of the art for LOM to achieve parts with 162 layers, over 1" thick, with multiple channels from 0.7-1.6 mm wide. Significant advances were achieved in laser cutting optimization, lamination techniques, and binder removal.

The concept of using an iterative process for the design and build of the heat exchanger was a key factor in the success of this program. Through modeling, the optimum materials and design criteria were selected. Rapid experimental build testing results were used to obtain next generation designs. It was found that a design for performance model (DFP) with 31 (cold side) – 39 (hot side) thin fins and channels required multiple internal support struts with ventilated sacrificial external fin supports. This was required to prevent distortion of fins during the build and to allow binder removal during firing. A modification was developed to simplify the part, called design for build (DFB), with fewer and thicker fins (16 each for hot and cold) and wider channels. This design was successfully built without the use of external supports and required fewer internal supports. These design protocols can be used in future development efforts for LOM applications.

Originally, it was envisioned that aluminum nitride (AlN) would be functionally graded with zirconia (ZrO_2) to achieve the material properties and sealing capabilities. It was found through modeling that the high thermal conductivity of AlN was less critical than initially anticipated. In addition, AlN was problematic to densify, requiring ultrahigh temperatures in inert atmosphere, which caused deleterious reactions with zirconia. A large body of work on the use of zirconia toughened mullite (ZTM), indicated its applicability for high temperature heat exchangers. ZTM has an added benefit of low cost, ease of densification and functional grading with zirconia. ZTM was down-selected and sufficient quantity of high quality ZTM tape was produced for prototype fabrication.

Three full size prototypes were produced, two using the Design for Build model, and one using the Design for Performance model. Characterization and sub-scale studies provided the understanding needed to build large parts. Two major challenges were encountered: large area lamination flaws and shrinkage cracking. Several techniques and design modifications were successfully implemented to mitigate these effects. This included lamination fluid control and adjusting the design to minimize large lamination surfaces. Shrinkage cracking was prevented through design modification, slow firing rate, and preventing surface drag during firing.

This study indicated that ZTM can be functionally graded to zirconia tubes for thermal expansion matching with the metal housing of a microturbine recuperator. However, functional grading was not required in this project, due to a novel approach that was developed for sealing the heat exchange core into the performance test rig. This entailed designing a core envelope to match the rig contours and mechanically sealing with a graphite gasket. This provided a versatile method for testing a variety of fin designs in the same rig, without the need for braze.

Testing successfully demonstrated that the prototype could withstand the high temperatures required for operation. Analysis showed higher than anticipated efficiencies due to cross-talk between the hot and cold flow channels. Micro computed tomography analysis was used to identify the cause as a small crack at the top fluid layers of the prototype. It is likely that this flaw was the result of stresses induced during handling of the green

part before firing. The first eight fluid layers were free of compromising flaws. The solution to enable building crack free taller parts, is the use of building with six fluid layer modules.

Information from the full size prototype build was used to envision a manufacturing process. This was accomplished by setting reasonable parameters for the number of parts based on demand, material and labor costs, and process speed. The scale up analysis focused on the production feasibility of 100 heat exchangers of 4 inch cube dimensions per month, based on the DFB design. The estimated cost to produce these parts was $1,200 per part. With a selling price recommended by the subcontractor of $4,000 per part, it appears that this approach is commercially viable.

This program successfully demonstrated feasibility of using additive manufacturing to fabricate high temperature ceramic heat exchangers, and advanced the Technology Readiness Level to level two with a clear path to achieve level three.

Task 1 – Project management

The work of this project was divided into five key tasks, with progress marked by the completion of sub-task milestones. The work plan was intentionally designed to allow feedback between process development and design optimization.

Task 1 – Project Management
Task 2 – Heat exchanger prototype design and modeling
  Task 2.1 – Thermo-fluid modeling
  Task 2.2 – Thermal stress model development
  Task 2.3 – Design optimization for prototype fabrication
Task 3 – Heat exchanger prototype sub and full scale fabrication
  Task 3.1 – Materials selection
  Task 3.2 – Sub-scale prototype fabrication
  Task 3.3 – Characterization report
  Task 3.4 – Full-scale prototype fabrication
Task 4 – System level challenge investigation
  Task 4.1 – Seal heat exchangers for testing
  Task 4.2 – Technology scale-up analysis
Task 5 – Heat exchanger prototype performance testing

The Project Management Plan included a reporting schedule, timeline, risk mitigation plan, financial plan, and success criteria. Table 1 gives a summary of the Milestone Completion Report. The tasks were successfully accomplished with a maximum of a 2 week delay for Tasks 2.1, 2.2, and 3.1. This was caused by a delayed start with the subcontractor, however, the PI succeeded in bringing the project back on schedule for an on time completion. A Risk Mitigation Plan was successfully implemented. Simplified methods for ceramic tape fabrication, densification, and sealing the ceramic into the rig were developed in this program. The need for functionally grading was eliminated by substituting zirconia toughened mullite (ZTM) - a more compatible ceramic - for aluminum nitride.

Table 1: Milestone Completion Report.

Task	Milestone	Completion Date		Verification Method/Success Criteria
		Planned	Actual	
1	Successful management of project.	10/28/15	10/28/15	Project completed on time.
2.1	Sub-scale heat exchanger prototype drawings	12/26/14	1/14/15	Complete set of drawings. Includes creation of LOM slice files.
2.2	Recommendations based on stress model results	2/28/15	3/27/15	Report with design modification recommendations.
2.3	Full-scale heat exchanger prototype drawings	4/29/15	5/19/15	Complete set of drawings based on scaling and model results. Includes creation of LOM slice files.
3.1	Ceramic tapes fabricated	1/2/15	1/21/15	Ceramic tapes procured. Enables prototype fabrication.
3.2	Sub-scale heat exchanger prototype fabricated	2/20/15	2/25/15	Laminated and sintered sub-scale prototypes produced.
3.3	Property characterization report	3/4/15	3/13/15	Report on quantitative materials properties.
3.4	Final heat exchanger prototype fabricated	7/29/15	7/30/15	Laminated and sintered full-scale prototypes produced.
4.1	Final heat exchanger prototype sealed	8/26/15	9/9/15	Full size prototypes sealed for heat exchange testing
4.2	Scale-up cost analysis report	9/10/15	9/9/15	Quantitative analysis of production costing, comparing current and estimated scale-up
5	Heat exchanger full-scale performance testing	10/28/15	11/11/15	Quantitative report of heat transfer capacity of the ceramic heat exchanger.

Task 2 – Heat exchanger prototype design and modeling

Experimental Methods

The subcontractor exercised its proprietary heat exchanger design tools to optimize the ceramic heat exchanger design for maximum effectiveness within the given design envelope, manufacturing constraints, and flow/ temperature conditions. First, the model was used to quantify the impact of heat exchanger material. Design parameters were varied to maximize the simulated effectiveness of the heat exchanger. The thermal conductivity (k) of the heat exchanger was varied while the fin design and inlet conditions were fixed. The fin design parameters were individually varied to determine the impact on heat exchanger effectiveness.

Finite element analysis was used to perform a thermal stress evaluation of the parameters used to define the core geometry of a ceramic heat exchanger. The results from the thermal stress sensitivity analysis were consequently used to understand the variation in the thermoelastic response of the core, when subjected to a non-uniform temperature change defined by the hot and cold side operating conditions. The analysis provided feedback and fin design constraints to the heat exchanger design for minimizing thermal stress during operation.

Finite element analysis was used to run a parametric sensitivity analysis which can be used to guide the optimization of the heat exchanger core geometry. A sequential process was implemented for adjusting fin design parameters and solving the thermal and mechanical models automatically. After the thermal model solves, the temperatures are written into the structural model which calculates the thermal strain. The results were then compared with the flexure strength of mullite. Mullite was used as a conservative estimate for the strength of zirconia toughened mullite.

Material properties were extracted from literature for the finite element models. The down-selected ceramic heat exchanger was modeled using Model Based Design tools which use analytical and numerical tools to optimize design for given volume and performance requirements or constraints.

For discussing the heat exchanger configuration and flow channels, a pictorial guide is given in Figure 1.

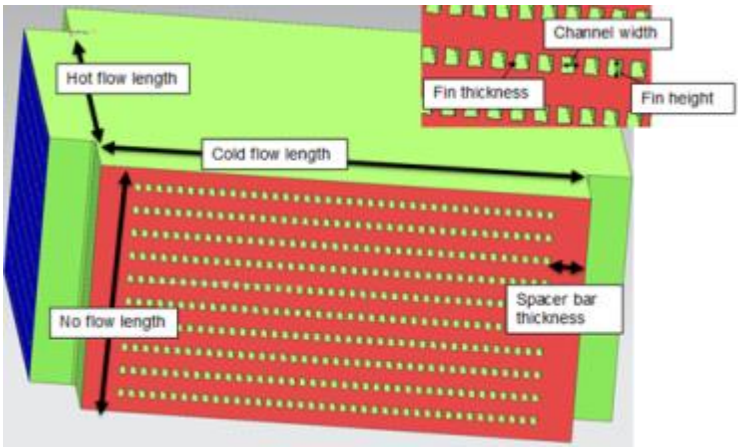

Figure 1: Definition of overall heat exchanger nomenclature.

Results and Discussion

Task 2.1 – Design and model development

A study was conducted on the effect of material thermal conductivity as shown below in Figure 2. For a fixed fin design, a diminishing increase in effectiveness was shown for thermal conductivity values greater than 30 W/mK (Figure 2 (left)). Optimized fin parameters (thickness, height, pitch) show a diminishing effectiveness benefit at much lower values of thermal conductivity, achieving a plateau more dependent on the pressure drop of the system (Figure 2 (right)). These studies affirmed that the performance impact of using a lower thermal

conductivity composite (e.g. 6 W/mK) as the heat exchanger material can achieve high effectiveness, provided that denser fin geometries are manufactured to compensate. In general, marginal gain in performance is noted once thermal conductivity is increased beyond 20 W/mK.

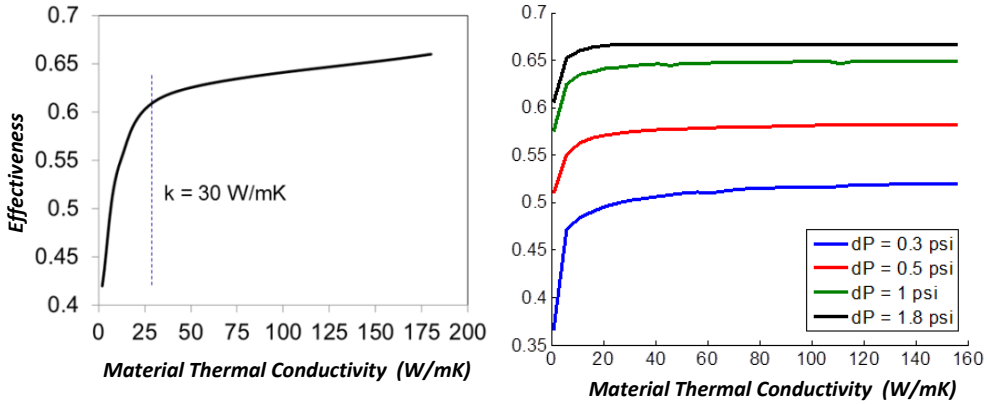

Figure 2: (Left) Effectiveness vs. material thermal conductivity for design pressure drop and fixed fin designs. Diminishing positive effect of increased thermal conductivity shown for >30 W/mK. (Right) Effectiveness vs. material thermal conductivity for various pressure drop constraints with fin design parameters optimized.

A study was completed to also determine the impact of fin geometry on the performance of the heat exchanger. Modeling verified that the effectiveness increases with heat transfer surface, as shown in Figure 3. With increasing fin thickness, the pressure drop also increased, and effectiveness decreased (Figure 3 (left)). As the channel gap (space between fins) increased, both the pressure drop and effectiveness decreased, as anticipated. This was quantified for the parameters selected in Figure 3 (right), demonstrating that small channels and thin fins provide optimal thermal performance. This is in contrast to the trends for structural strength, which will be discussed in the following section.

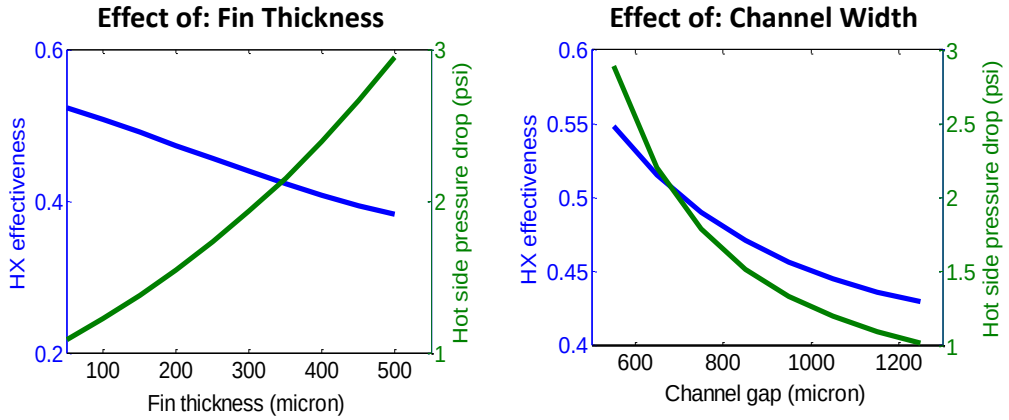

Figure 3: (Left) Result of changing fin thickness on effectiveness and pressure drop at fixed channel gap. (Right) Result of changing channel gap on effectiveness and pressure drop at fixed fin thickness.

Task 2.2 – Thermo-fluidic and stress modeling

The material property values for mullite, Table 2, were used for the thermo-fluidic and stress modeling as conservative values (for strength) to represent zirconia toughened mullite (ZTM). A baseline design was determined to yield the maximum thermal performance and effectiveness for the cross-flow configuration. This design is a single module of the overall heat exchanger used for evaluation and sensitivity analysis. A visual of the baseline and values of its dimensions are given in Figure 4.

Table 2: Mullite Material Properties at room temperature.

Property	Value
Coefficient of thermal expansion	5.4E-6 1/C
Thermal Conductivity at 20 °C	6 W/(mC)
Thermal Conductivity at 1400 °C	3 W/(mC)
Young's modulus	5.4E6 MPa
Poisson's ratio	0.22
Flexure Strength	170-180 MPa
Compressive Strength	550-1310 MPa

(Note: the strength value of mullite gives the worst case scenario, ZTM can achieve a stregnth of over 300 MPa)

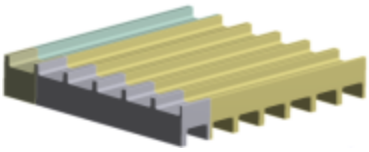

Dimensions	Hot Side	Cold Side
Fin Thickness (µm)	200	200
Fin Height (µm)	1000	600

Figure 4: 3D Solid model representation of core section with baseline dimensions.

Thermal Finite Element Model

A symmetric finite element model of the flow channels of the heat exchanger core was created. A uniform temperature was applied to the mid-plane surface of the model with symmetric boundary conditions. In a cross-flow heat exchanger configuration, the corner with the hot in-flow and cold out-flow experiences the highest temperature gradient. In order to approximate this phenomenon, the outer most internal fins of the geometry are modeled as half the width of the other fins. These half-walls are also used to apply structural symmetry at this location. This produces a thermal gradient that normalizes towards the center of the core, as would be expected in operation. Figure 5 shows the modeling results. Having a clear understanding of the temperature gradient in the plate and fins is necessary for predicting the thermal expansion induced stress during operation.

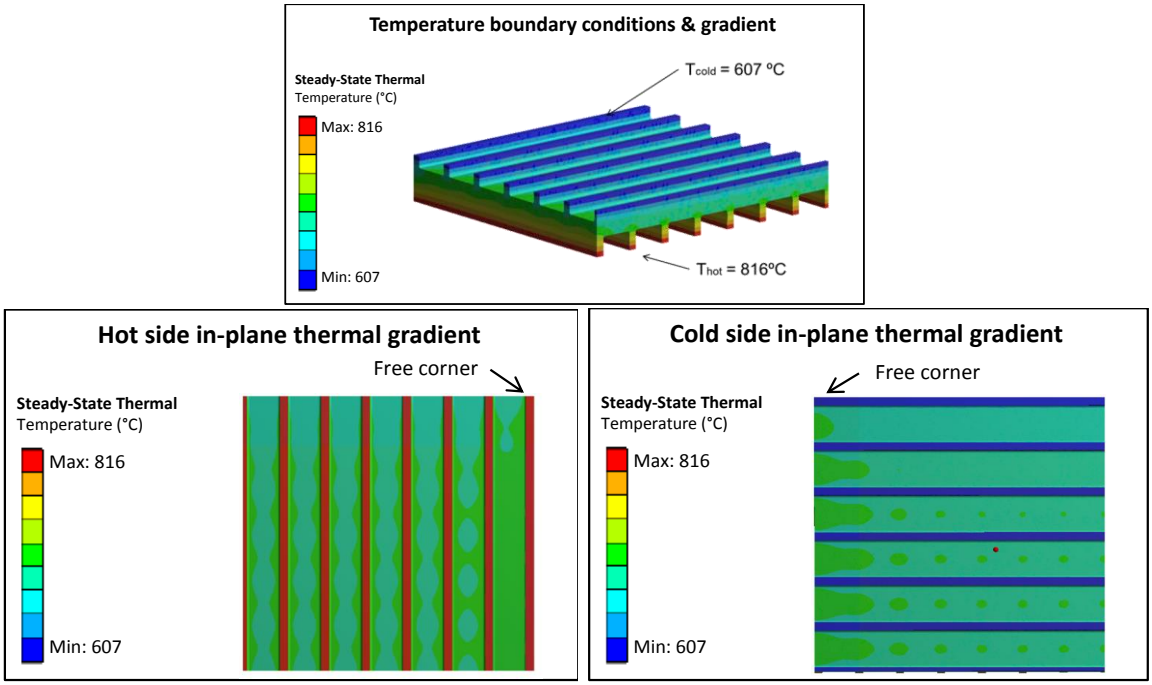

Figure 5: Model results: (Top) Overall output showing temperature gradient. **(**Left) Hot side in-plane thermal gradient, half-width fin shown on the left side. (Right) Cold side in-plane thermal gradient, half-width fin shown on the bottom. The corner with the hot in-flow and cold out-flow (free corner) experiences the highest temperature differential.

Structural Finite Element Model

Modeling was performed to show the predicted deformation associated with thermal expansion of the ceramic. The structural finite element model incorporates symmetry boundary conditions on the fin mid-planes and internal walls of the heat exchanger. These boundary conditions set in-plane displacements and out of plane rotations equal to zero. This allows the model to grow in the direction indicated in Figure 6 (left), while the fin mid-surfaces remain in-plane. The through thickness deformation is shown below in Figure 6 (right).

Examination of the 84X magnified through thickness deformation (see Figure 6 (right)) contour plot of the hot-side inlet, illustrates the thermal bending observed by the hot-side inlet separator plate, and the hot-side wall of the core. This bending is due to the high temperatures at this location, and a restriction of thermal growth through the thickness, by use of the symmetry conditions on the mid-plane fin surfaces. This bending is the source of the maximum stresses in that specific corner, as discussed in the following sections. In addition to recording the stress in the hot-side corner, the cold side of the corresponding corner is also monitored in the sensitivity analysis (location of interest).

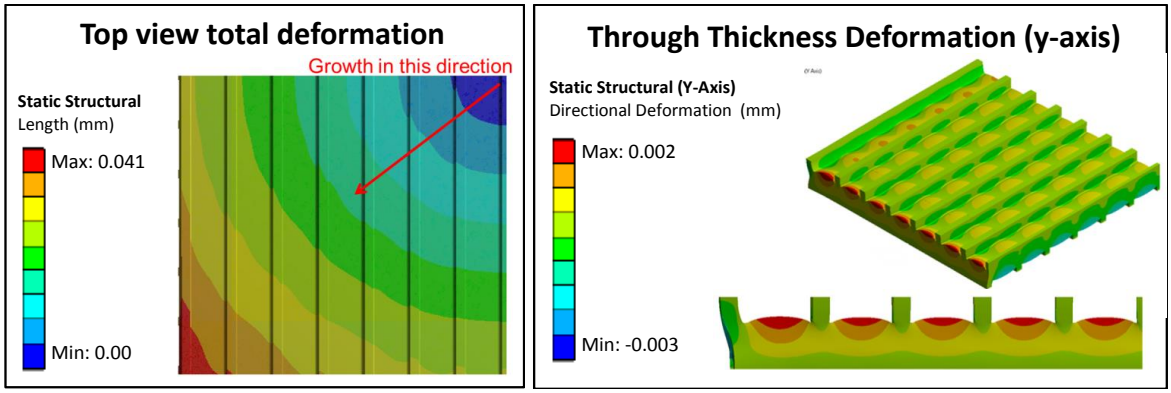

Figure 6: (Left) Total deformation at steady-state, maximum deformation of 0.041 mm. (Right) Y-axis deformation at steady state, maximum deformation of 0.002 mm.

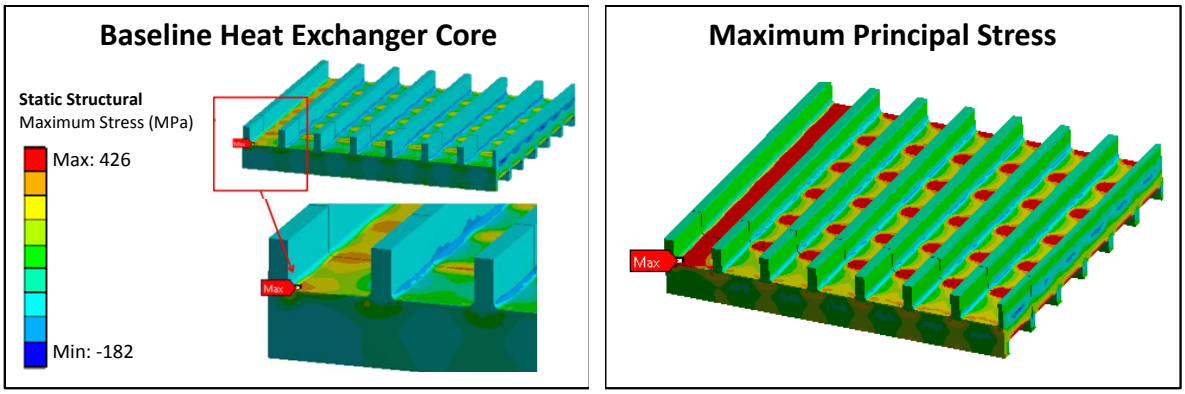

Figure 7: (Left) Model output for baseline heat exchanger core showing close view of maximum stress corner. (Right) Maximum principal stress along hot side base plate (426 MPa). The indicated corner is the location of interest for the parametric sensitivity analysis.

The calculated maximum principal stress is 425 MPa, given the applied thermal gradients and constraints of the baseline configuration. The flexure strength of one of the candidate material (mullite) as reported in Table 2 is 180 MPa. Figure 7 (right) shows the locations of the core that have stresses above 180 MPa (strength of mullite) shown in red.

In order to reduce the stress of the heat exchanger core, a sensitivity analysis was performed that varies dimensional parameters and records the variation of stress at the location of interest. The sensitivity analysis holds the baseline dimensions constant while varying one parameter to illustrate the effect of the stresses of the core to changing the specified parameter. The stresses as a function of hot and cold side fin thickness (Figure 8), fin height (Figure 9), operating temperatures (Figure 10) and cold side channel width (Figure 11) are reported below.

Some numerical noise is observed in the finite element model which has been confirmed to be a phenomena of a different mesh for each load case; however, the trends are still evident.

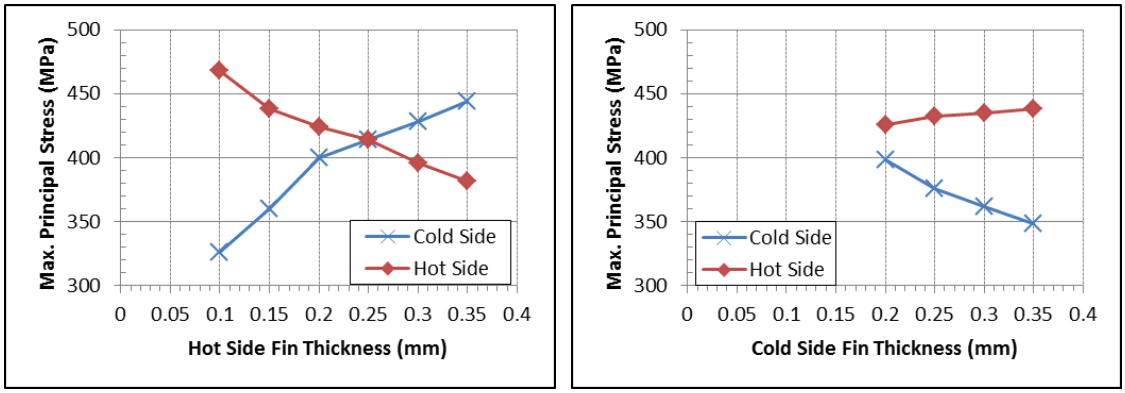

Figure 8: Stress as a function of hot side fin thickness (left) and cold side fin thickness (right). Increasing the thickness of the hot fin decreases the stress in the hot channel, while increasing cold channel stress. A similar trend is shown for increasing cold side fin thickness, decreased cold side stress with increased hot side stress for thicker fins. This indicates that there is likely an optimized ratio of hot to cold side fin thickness for a given temperature difference.

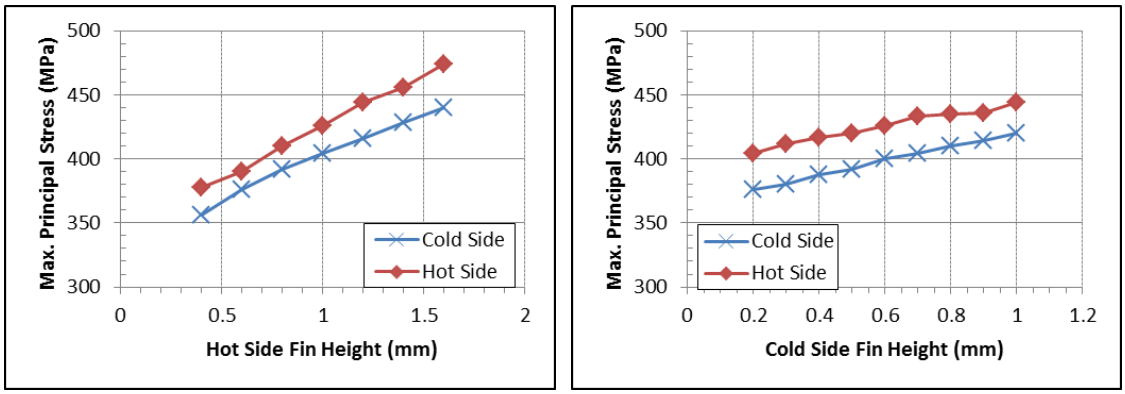

Figure 9: Stress as a function of hot side fin height (left) and cold side fin height (right). Both show a trend where taller fins increase stress.

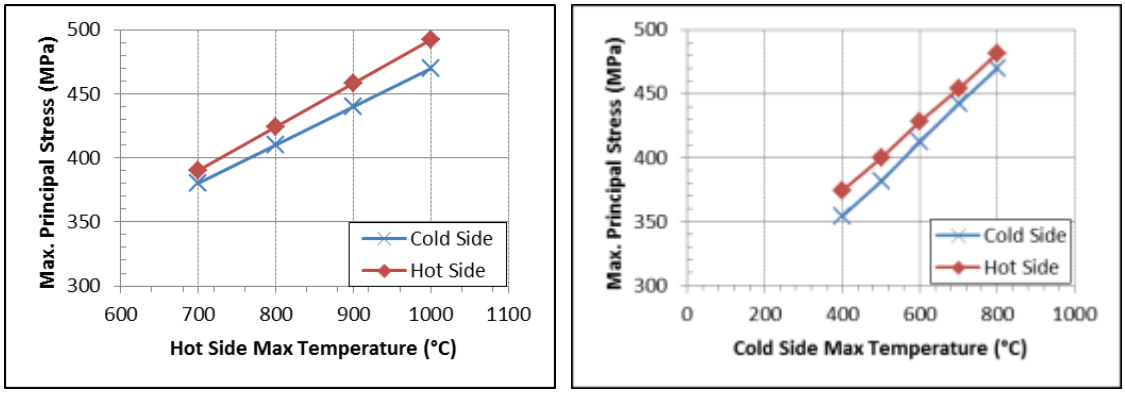

Figure 10: Stress as a function of hot side temperature (left) and cold side temperature (right). Both show a trend where higher temperature results in higher stress.

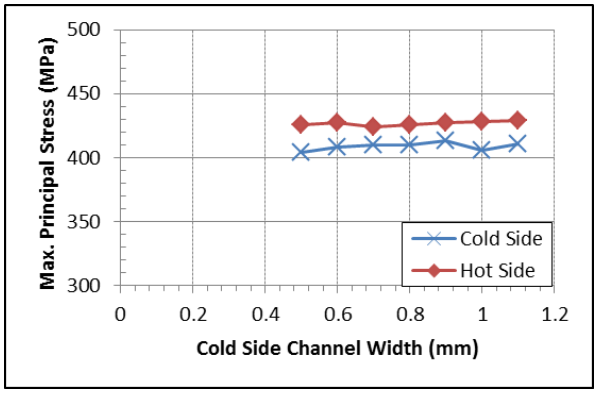

Figure 11: Stress as a function of cold side channel width showing a negligible difference in stress.

As a result of this analysis, the thermo-fluid heat exchanger design optimization model was re-exercised with new design bounds for the heat transfer fins. Higher fin thickness and lower fin heights were used to obtain an optimized heat exchanger design for maximum effectiveness which also meets the maximum stress criteria. A heat exchanger prototype model was then provided with the new optimized design. This design showed a maximum thermal stress value below 300 MPa, which can be sustained by zirconia toughened mullite.

The temperature profiles and boundary conditions used in the model are conservative, but offer sufficient insight into the thermal-elastic response of the heat exchanger's core. The trends provided from the sensitivity analysis were used to identify an ideal combination of fin design parameters that produce optimized efficiency and provide an easier path towards fabrication.

Task 2.3 – Final design optimization

The heat exchanger design cycle is shown in Figure 12 broken into the primary design steps. First, the heat exchanger material was down-selected based on properties and manufacturability. Then the ceramic heat exchanger was modeled using Model Based Design tools which use analytical and numerical tools to optimize design for given volume and performance requirements or constraints. The design space was explored to determine the optimal design to meet performance goals. A design with modified plain fins was selected for manufacturability. Thermal stress analysis was performed on the optimal fins. To reduce the stress on the fins, the design was changed to use thicker and shorter fins. The final prototype design was re-optimized with all the manufacturing constraints and thermal-stress analysis results.

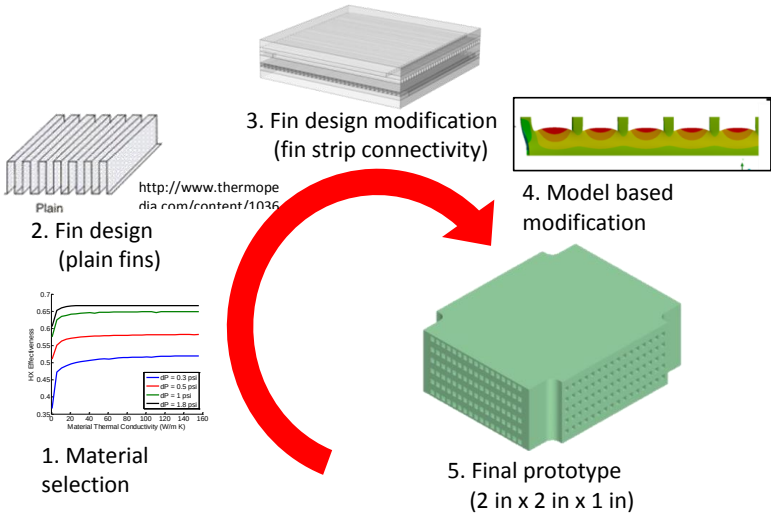

Figure 12: Heat exchanger design cycle balancing manufacturability and performance optimization.

The target operating conditions are as follows:

Table 3: Target operating conditions for the hot and cold sides of the cross-flow heat exchanger

	Hot Side	Cold Side
Mass Flow (pounds per second)	0.025	0.025
Inlet Temperature (°F)	1500	401
Inlet Pressure (psi)	20	58
Target Pressure Drop (psi)	1.75	1.75

The minimum fin thickness was 0.40 mm. Thinner fins have been demonstrated (0.20 mm) at a sub-scale. The thinner value was not selected based on manufacturing constraints and stress requirements. It also helps to keep the stresses in the corners of the fins low. The solid model was generated with dimensions after the firing is complete.

Through the previous analysis, for the 4x4x4 inch design volume, a baseline design was determined to yield the maximum performance and effectiveness for the cross-flow configuration. Given the manufacturing constraints feedback from the sub-scale fabrication trials, only plain fins were considered for the baseline optimized designs.

The heat exchanger prototype envelope and fin designs were further refined, with modifications iterations between modeling and build testing used to quickly adapt the design. The two final designs described below are the design with maximized performance (DFP) featuring thinner fins and channels, and a design for build (DFB) with thicker taller fins with wider channels (Figure 13).

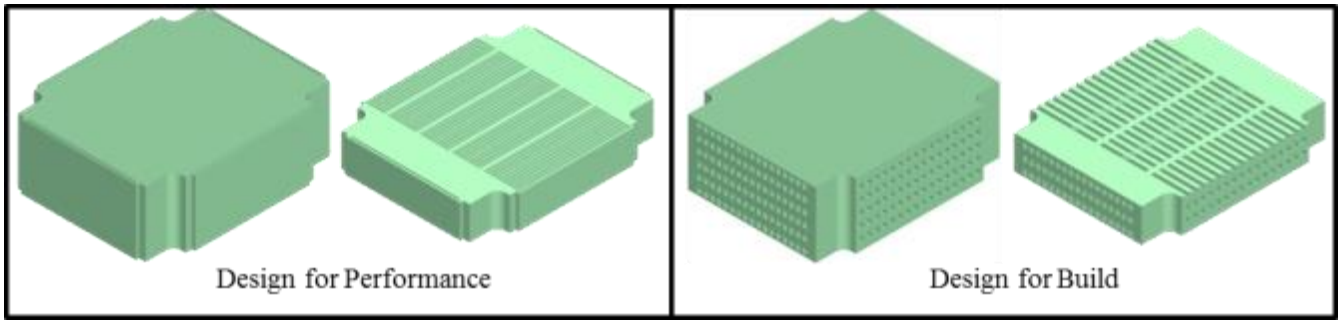

Figure 13: Left- Design for Performance (DFP), Right- Design for Build (DFB), models.

A summary of the defining characteristic dimensions are given below in Table 4. Both of these designs feature a hot and cold flow-length of 2 inches, and a no flow length of 1 inch.

Table 4: Summary of comparative values for DFP and DFB

	Design For Performance (DFP)		**Design For Build (DFB)**	
	Hot Side	Cold Side	Hot Side	Cold Side
Number of Fins	39	31	16	16
Fin Width	0.4 mm	0.4 mm	1.0 mm	1.5 mm
Fin Height	0.80 mm (5 layers)	0.32 (2 layers)	1.92 (12 layers)	1.92 (12 layers)
Channel Width	0.7 mm	1.0 mm	1.6 mm	1.5 mm

The thermal performances comparing DFP and DFB configurations from the model are given in Table 5. Maximum pressure drop constraint of 1.8 psi was applied on both the hot and cold sides. Maximizing the total heat transfer/ effectiveness was set as the objective for optimization. The maximum theoretical effectiveness of 0.49 with plain fins can be achieved, in comparison to the theoretical strip-fin design effectiveness of 0.65.

Table 5: Performance predictions comparing Design for Performance with Design for Build configurations

	DFP	DFB
Hot dP (psi)	1.75	1.23
Cold dP (psi)	1.68	0.42
Effectiveness	0.38	0.17
Q (kW)	2.81	1.20

The DFP small flow channels caused high pressure drops at the target flow conditions. Therefore, taller fins were selected. Compared to the baseline, the separator plate thickness was increased to reduce the maximum corner stress. The final thermal-stress analysis predicts the max corner stress to be 385 MPa and the max bulk stress to be 305 MPa. Corners were further filleted to reduce the corner stress below 300 MPa.

A design feature that was included for manufacturability is internal struts that are perpendicular to the flow direction. To allow flow to pass through the channels, the support struts were offset at half of the fin height resulting in a 3D zig-zag flow pattern. A conjugate heat transfer (CFD) analysis was performed to study the impact of the zig-zag flow pattern on the heat transfer and pressure drop performance of the heat exchanger. Only one channel was modeled and a substantial increase in pressure drop was predicted with a moderate increase in heat transfer rate.

In addition to the internal support struts, sacrificial external support struts were developed to provide fin-end support during the build process, and to allow channel ventilation during firing. These sacrificial struts were designed to be easily removed after firing. This final DFP solid model was used for prototype manufacturing (Figure 13- left).

An additional design was developed with fin and channel dimensions selected for manufacturability based on build tests. The preliminary model was optimized giving rise to the design for build, or DFB, model (Figure 13- right). Due to the thicker, sturdier fins, no external sacrificial struts and fewer internal struts and were required for this model. A comparison of the DFP and DFB final dimensions is presented in Table 6.

Table 6: DFB design evolution from DFP featuring 6x taller and 4x wider fins

	Cold Side Fins		Hot Side Fins		Separator Plate
	Width (mm)	Height (mm)	Width (mm)	Height (mm)	Thickness (mm)
DFP Rev C & D	0.4064	0.32 (2 layers)	0.4064	0.80 (5 layers)	0.64 (4 layers)
Manufacturing Model	1.00	0.80 (5 layers)	1.00	1.92 (12 layers)	0.31 (2 layers)
DFB Model Optimized	1.6 (0.06")	1.9 (0.075")	1.00 (0.40")	1.9 (0.075")	0.32 (2 layers)

Figure 14 illustrates how the ceramic prototype core is oriented in the testing rig. The rig was designed to accept a variety of internal fin structures.

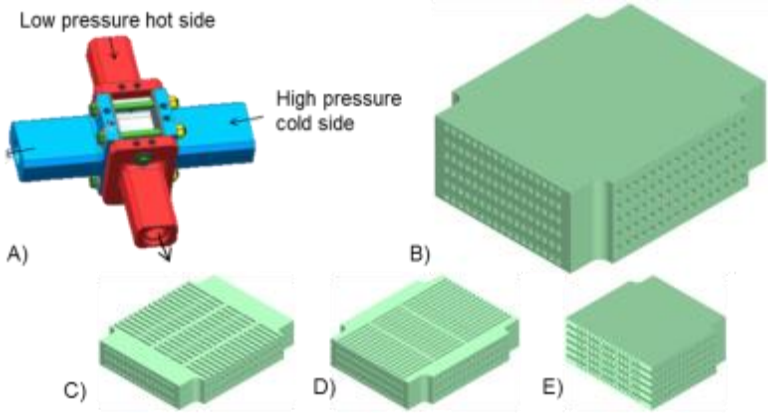

Figure 14: Selected final prototype design. A) Illustration of ceramic prototype core mechanically sealed into the rig, highlighting the hot and cold flow paths. B-E) Design For Build views of heat exchanger core.

Task 3 – Heat exchanger prototype fabrication

Experimental Methods

Down-selecting the material required laboratory investigation into different ceramic mixtures, specifically aluminum nitride (AlN)/zirconia (ZrO_2) and mullite/zirconia, to assess their suitability for the intended heat exchanger application. Ceramic powders were blended by ball milling, sieved, and pressed into sample pellets using a uniaxial press. Firing studies were performed to find the optimum firing temperature for full density. Density was measured by the Archimedes method and mass/volume. X-ray diffraction (XRD) analysis was used to determine post-firing composition.

Ceramic tapes were produced by ball milling the ceramic powders with solvent, binders, plasticizers, and dispersant, and then casting on polyethylene film. Several ceramic tape compositions were explored for functional grading and co-firing compatibility experiments.

The composition tests were used in conjunction with material property modeling from Task 2 to down-select zirconia toughened mullite. A sufficient quantity of tape was produced for prototypes. The flexible green tape was extremely uniform with a thickness at 0.22 mm.

Laminated object manufacturing (LOM) was used as the primary means of sample fabrication, along with the development of a large part firing profile. LOM was accomplished by use of a machine called the CAM-LEM (see Figure 15) at the prime contractor's facility. This machine takes 3D or 2D computer model files and breaks them into layers the thickness of the selected tape material. The ceramic tape is used as a feedstock for this machine. The machine individually CO_2 laser cuts each successive layer of the model, and precisely stacks, gradually building up the 3D part. The operating engineer controls the cut-tape cleaning using compressed air, and applies lamination fluid prior to stacking.

Figure 15: CAM-LEM machine.

Early laminated tape samples were analyzed by cutting open small samples with a diamond circular saw to examine the lamination between layers, via optical and scanning electron microscopy.

For full-size prototype samples, various design aspects were assessed through CAM-LEM building, and firing tests. The key areas examined were green removal of sacrificial struts by use of a ceramic blade, saw, and end mill; modular assembly of green prototype sections; and ventilated sacrificial strut build and firing testing. A firing shrinkage study used various setting powders, firing surfaces, and mobile media beds to assess the best method for firing large samples. The binder-removal and firing schedule was progressively refined for larger samples throughout the project.

Results and discussion

Task 3.1 – Material selection

The first major task was to down-select a material for the development of the prototype. The relevant properties of the main candidate materials are given in Table 7.

Table 7: Material properties of candidate materials (Note: properties at room temperature)

	Aluminum Nitride	Zirconia	Mullite	ZTM
Thermal conductivity (W/mK)	150-180	2.5-3.0	3.5	2.8-3.2
Thermal expansion (µm/mC)	5.0	11.0	5.3	7.2 [1]
Strength (MPa)	300-430	700-900	170-180	320-340
Fracture Toughness (MPa $m^{½}$)	2-3.5	6-9	1.9[1]	3.6[1]
Density (g/cm^3)	3.25	6.04	3.16	3.74

From initial work, it was envisioned that aluminum nitride (AlN) would be functionally graded to zirconia (ZrO_2). Since zirconia has a good thermal expansion match with Inconel, this would allow the heat exchanger to be

brazed directly to metal connector tubes. AlN has a high thermal conductivity, with was thought to be critical. Zirconia toughened mullite (ZTM) was another candidate extensively studied for compact high temperature heat exchangers [1-3].

Aluminum nitride is known to be a challenging material to work with. It has highly covalent bonding and requires ultra-high temperatures and sintering aids to achieve full density. Additionally, it reacts in humid conditions at room temperature, and has a tendency to react with oxides during firing. The high thermal conductivity of up to 180 W/mK is dependent on optimum processing conditions. This theoretical value is in excess of diminishing returns threshold value (20 to 30 W/mK) identified during the modeling investigation (Section 2.1).

Research from Naval Research Laboratories and the Imperial College London indicated that a low thermal conductivity allowed a thermal gradient that enhances heat flow.[1-3] In addition, convection in the open space was found to be more significant than thermal conductivity through the heat exchanger material. This information along with the material properties for ZTM composite was provided to the subcontractor to evaluate the candidacy of ZTM with thermal modeling in Tasks 2.1 and 2.2.

AlN and ZTM firing studies were performed to assess the densification and compatibility with zirconia. Aluminum nitride pellets were fired side-by-side with zirconia pellets to 1800 °C in a nitrogen atmosphere. This study incorporated AlN, AlN with yttria (Y_2O_3) as a sintering aid, AlN zirconia mixtures, and zirconia. A second study was performed with mullite zirconia mixtures using two different sources of mullite fired to 1550 °C in air. The results of this study are presented in Table 8.

Table 8: Summary of pellet firing study comparing pressed and cold isostatically pressed (CIP) pellets.

Material Composition (volume %)	Firing Conditions	Δ D		Th. Density (g/cc)	% Th. Density	
		(Pressed)	(CIP'ed)		(Pressed)	(CIP'ed)
AlN	1800 °C, 1 hr, N_2	3%	2%	3.26	68%	71%
AlN 97% + Y_2O_3 3%	1800 °C, 1 hr, N_2	10%	8%	3.29	81%	84%
AlN 76% + ZrO_2 24%	1800 °C, 1 hr, N_2	12%	10%	3.92	91%	93%
AlN 51% + ZrO_2 49%	1800 °C, 1 hr, N_2	16%	14%	4.61	98%	94%
ZrO_2	1800 °, 1 hr, N_2	22%	16%	6.05	99%	99%
Mullite(1) 80% + ZrO_2 20%	1500 °C, 4 hrs, air	5%	*N/A*	3.45	75%	*N/A*
Mullite(2) 80% + ZrO_2 20%	1500 °C, 4 hrs, air	14%	*N/A*	3.45	92%	*N/A*
ZrO_2	1550 °C, 4 hrs, air	22%	*N/A*	6.05	100%	*N/A*
Mullite(2) 80% + ZrO_2 20%	1550 °C, 4 hrs, air	16%	*N/A*	3.45	99%	*N/A*

Zirconia all is yttria partially stabilized zirconia.

The AlN/yttria samples achieved a maximum density of 81%, indicating that higher temperatures and longer hold times would be necessary to fully densify. The zirconia samples over-sintered and were subject to strength limiting exaggerated grain growth. The mullite/zirconia mixture samples showed that a fine grain mullite achieved 99% densification, and good compatibility with zirconia firing temperatures. The firing temperature for the ZTM system is 250 °C lower than that required for AlN and uses air instead of a controlled atmosphere furnace. This has a significant impact on the manufacturing cost.

Samples of green AlN and zirconia tapes were laminate and fired together, in several experiments to explore co-firing compatibility. The results showed curling and shattering of samples, which is consistent with stress induced by the different expansion and shrinkage factors.

A similar study was performed to examine the direct-lamination compatibility of zirconia and ZTM. A green pressed ZTM pellet was fired directly in contact (no lamination fluid) with a green zirconia tape. The fired sample showed that the tape and pellet adhered to each other. The difference in shrinkage caused a build-up of stress that resulted in cracking after cooling. The ZrO_2 tape, however, adhered and was well bonded with the ZTM, shown below in Figure 16. The thickness of the layer of ZTM was approximately four times the thickness of an individual layer of tape. The actual lamination and part build would therefore require a maximum of two functional grading steps to successfully bond the ZTM core to the zirconia connector tubes. It is anticipated that a

composition of zirconia/mullite of 50/50 and then 80% zirconia/20% mullite will be sufficient for bonding. This shows promise for functional grading ZTM to zirconia.

Figure 16: Mullite from pellet adhered well to ZrO_2 ceramic tape after firing showing good compatibility.

Analysis of the AlN/zirconia composite fired pellets by x-ray diffraction (XRD) shows that the aluminum nitride and zirconia composites reacted during the firing process (see Figure 17). The conditions for densification caused reactions that appear to prohibit functionally grading of AlN with zirconia.

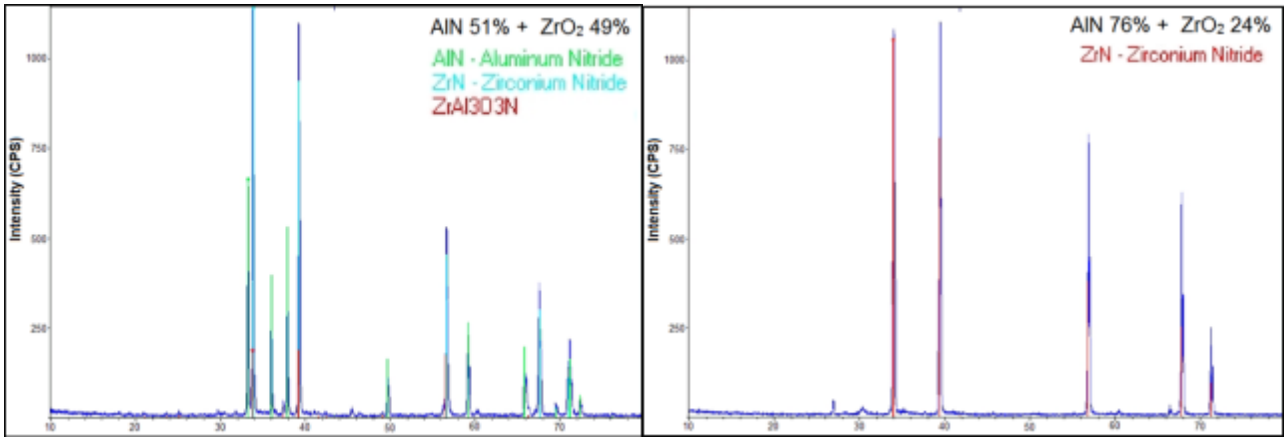

Figure 17: XRD analysis of AlN/zirconia pellets. (Left) XRD of 51% AlN pellet showing a high content of reacted material, and minimal or no residual zirconia. The reacted materials are zirconium nitride (ZN) and zirconium aluminum oxynitride ($ZrAl_3O_3N$) phases. (Right) XRD of 76% AlN pellet showing almost all of the material reacted to zirconium nitride at the surface where the measurement was taken.

Following the investigation of candidate materials, zirconia toughened mullite was selected as the material providing the highest confidence for success. From this selection, sufficient tapes were fabricated for prototypes building.

A ZTM firing study was conducted to optimize the density. Table 9 shows the results with the optimal firing temperature of 1550 °C, with the samples achieving 99% density.

Table 9: Firing Temperature Study Results

	1570 °C	1550 °C	1500 °C
% Theoretical Density	96%	99%	98%

Task 3.2 – Sub-scale prototype fabrication

Laminated object manufacturing (LOM) is capable of producing fine features with a high degree of accuracy; however the desirable features for the heat exchanger push the limits of manufacturability. A simple robust design was constructed to explore the materials handling challenges. A nature inspired honeycomb structure with offset layers for airflow channels was built using LOM as pictured in Figure 18. This is a complete heat exchanger with

cold and hot flow channels. The 11 tape layer structure was fired successfully to high density. The building of this first prototype enabled a better understanding of the process parameters. Feedback was provided to the subcontractor on the manufacturability issues of structures with different types of connectivity between layers and internal structure.

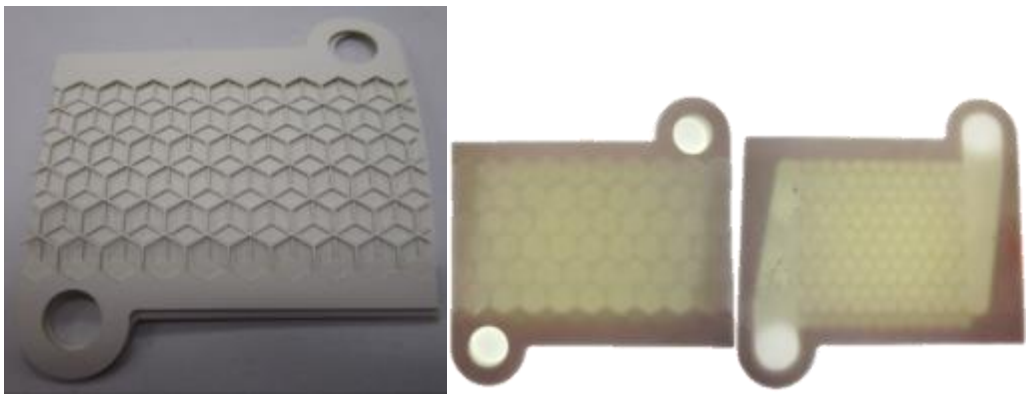

Figure 18: Sub-scale prototype heat exchanger with one hot and one cold flow channel. The structures were cut into green ceramic zirconia toughened mullite (ZTM) tapes, using 11 separate tape layers. This design illustrates complex and precisely cut fine features with high connectivity lending stability to the individual layers. (Left) Green structure before manifold layer was applied. (Right) Fired ceramic heat exchanger prototype.

Task 3.3 – Characterization

Results from this task were compiled in a characterization report, given in Appendix A. Key problems were identified and solved through process and design adjustments:

- Full density was achieved by choosing fine grain starting materials and adjusting the firing schedule.
- Tape distortion was remedied by control of lamination fluid during stacking.
- Macroporosity causing delamination was eliminated through decreasing the binder burnout rate.
- Micro-delamination caused by fine particulates was addressed by implementation of a cleaning procedure prior to tape stacking. This was successful in solving delamination in small scale samples.
- Distortion of fine features was caused by:
    1) Unsupported heat exchanger fins → mitigated by design optimization
    2) Transport of cut tapes → minimized by design and process improvements
    3) Friction of part during shrinkage → solved by use of smooth firing surface in small samples

The enormous advances in the fabrication process during this project have resulted in the improvement of the lamination procedure to such a degree that previously the cleaned tape results (5% linear delamination) are now comparable to current un-cleaned tape results. Process refinements throughout successive builds were able to achieve similar improvements to larger scale samples than those examined for the characterization study. Ultimately, full scale prototypes were fabricated without the use of a cleaning step due to sufficient process improvement.

A manufacturing concern for LOM is the successful lamination of large surface area sections or layers. This is challenging due to the flexible nature of the ceramic tape and high degree of manual operation required at this stage of the development process. These factors can cause air or fluid bubbles to become trapped between the tape layers that prevent effective local green lamination. During firing, the bubbles can rupture and create fractures, or localized delamination. This information was fed back to the design cycle to minimize dead space. In addition, strategies for stiffening the tape were developed. These include tape binder modification and decreasing the temperature during the build process.

This characterization task was used to understand and develop novel processing methods and designs that enable the fabrication of a complex ceramic heat exchanger. This work advances the understanding of ceramic additive manufacturing.

Task 3.4 – Full-scale prototype fabrication

Throughout the final design selection process, studies were performed to understand the impact of design and fabrication factors, to optimize the quality of the prototypes. The major flaws, which occurred as the part size was scaled up, were primarily bottom tearing and corner cracking. To a lesser degree, delamination and trapped air bubbles were observed. The flaws were examined and found to have multiple causes: 1) part-envelope design caused corner cracking, 2) shrinkage and drag on firing surface caused bottom cracking, 3) aggressive firing schedule caused uneven shrinkage and outgassing cracks, 4) build technique caused imperfect layer alignment and trapped air bubbles. The studies performed to understand and remedy these LOM challenges are discussed in this section.

Part Envelope Design

A full size design for performance (DFP) prototype was successfully built and fired (see Figure **19**) using the lessons learned building smaller parts. Corner cracking was observed, prompting a design modification with a larger radius corner fillet.

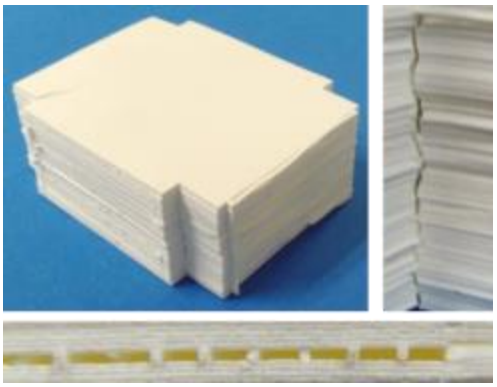

Figure 19: Full size fired part with ventilated sacrificial strut. Shown are an overall view of the fired part, a close view of the corner, and a close view of the top set of channels. The part is well fired, however it contains a large corner crack.

The full-scale prototype was successfully built and fired with the minor defect of corner cracking shown above (Figure 19). This flaw was resolved by modifying the corner to a larger radius curve. A test build of the updated corner model was completed to verify that this modification would be successful at preventing corner cracking of a full sized prototype (see Figure 20).

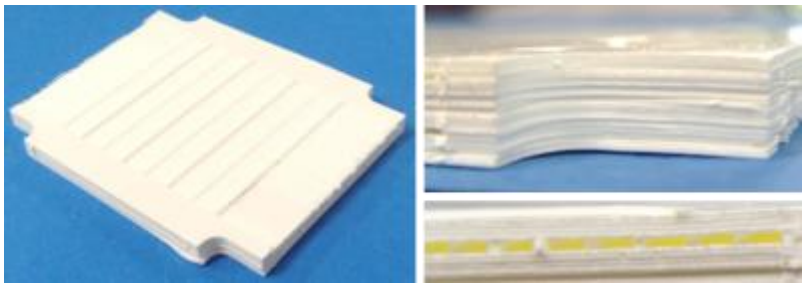

Figure 20: Test build of the updated prototype design with rounded corners. Shown are the overall external view, corner view, and close view of channel opening. This sample shows no corner cracking, validating the modification for full-sized testing.

Shrinkage Drag

The firing surface is a critical aspect of processing that can cause or prevent flaws in the final prototype. The ceramic part exhibits a high linear shrinkage of 26-27% in the XY plane. This can lead to tearing or cracking during shrinkage drag. These flaws are due to the mass of the part combined with the fragile nature of the ceramic after binder removal and before densification, as the part shrinks and drags along the firing surface. Early firing

surface studies identified the two best candidates during firing as a mobile media bed and mullite setting powder. These results were determined from small samples prior to testing on larger samples.

The results of the media bed experiments showed promise, but were not an ideal solution for larger parts. The media seized up and sintered to the bottom of the parts in places, causing immobility, dimpling and tearing (see Figure 21).

Figure 21: Results of mobile media bed experiments. (Left) Small media bed – sample bottom with cracking and media sintered to sample. (Center) Large media bed – full size part. (Right) Close up of B bottom – dimple in lower right shows where the media adhered to the part.

Mullite setting powder was more successful at preventing bottom cracking in large parts. A study testing a wide range of mullite grain size powders and setter materials was conducted. It was found that -325 mesh high purity mullite setting powder greatly reduced the severity of the cracks. Further refinement of the firing process was necessary to completely eliminate these flaws. Residual mullite powder that sintered to the bottom face of the part was easily removed with gentle grinding.

Firing schedule

In the characterization study (Task 3.3) it was found that a binder removal rate of 1°C/min was sufficient for small samples. By increasing the size of the prototype, flaws associated with overly rapid binder removal, such as delamination pockets and cracks, were observed. The binder removal heating rate was decreased to 0.3 C/min and a dwell stage was added, which eliminated these flaws. A slower binder removal schedule also ensured a uniform temperature distribution throughout the larger parts, reducing the risk of uneven shrinkage caused by internal temperature gradients.

Final Prototype Builds / Build Technique

Progressive development of part building technique was a key area that enabled full size prototype fabrication. Two parallel paths were explored during the course of this program: design for performance (DFP) (Figure 22), and design for build (DFB) (see Figure 23 and Figure 24). Both of these design models were used in the predictive performance analysis in Task 2. Both prototypes were built, however, DFB was more robust and became the focus for testing and analysis. None the less, strategies for DFP were greatly advanced, and will be important in the future development of high performance ceramic heat exchangers.

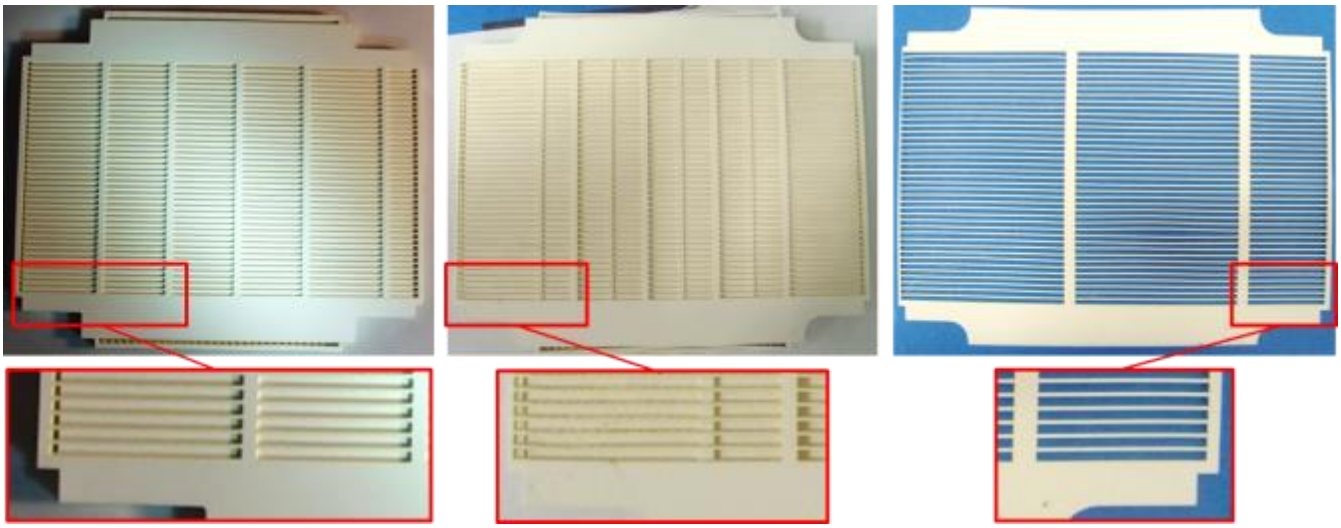

Figure 22: Evolution of the DFP fin design. (Left) hot fluid layers mid build, showing 5 internal struts and ventilated external sacrificial strut. (Center) DFP design modification mid build, 8 internal struts creating a zig-zag flow path. (Right) Test cut layer showing same fin and channel widths, with fewer internal struts.

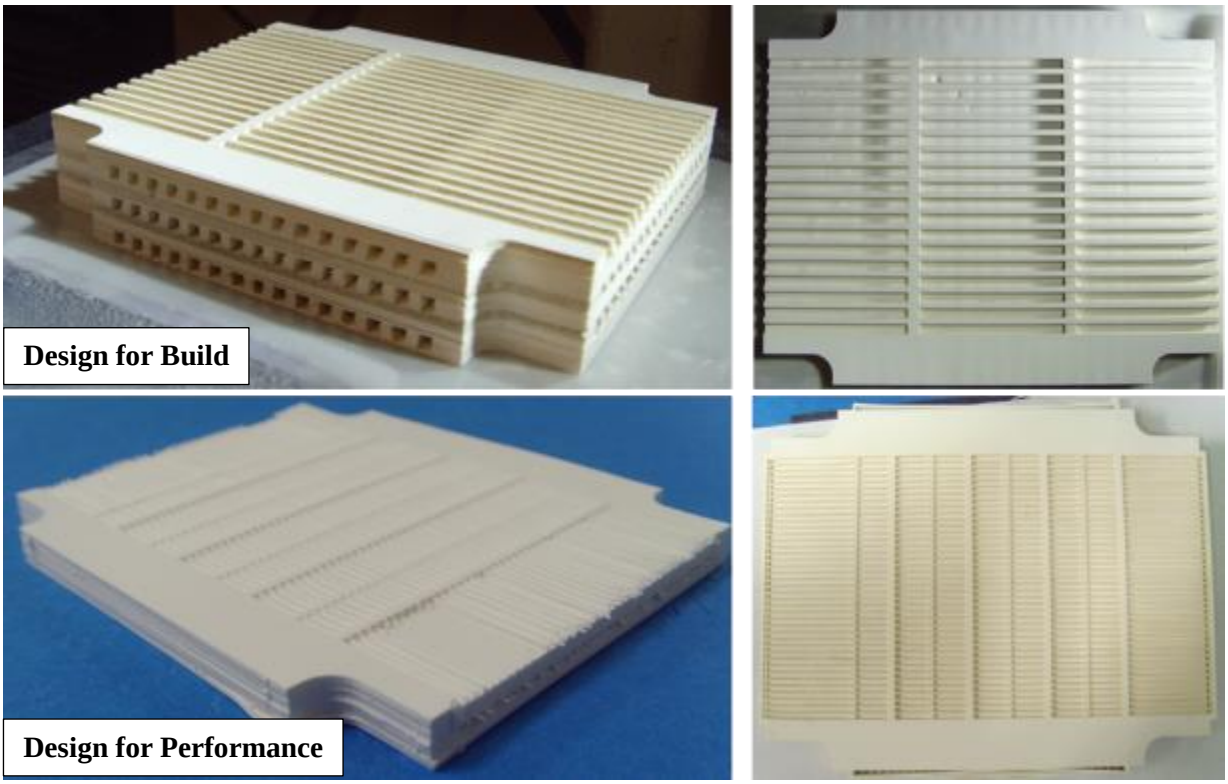

Figure 23: Pictured is a comparison of the DFB and DFP prototypes mid-build. (Top) DFB prototype large open channels and thick fins, no external strut. Top-down view shows zig-zag flow path created by two internal support struts, visible by shadow strut casts on separator plate. (Bottom) DFP prototype 30 layer sample. Top-down view shows thin fins and 8 internal struts.

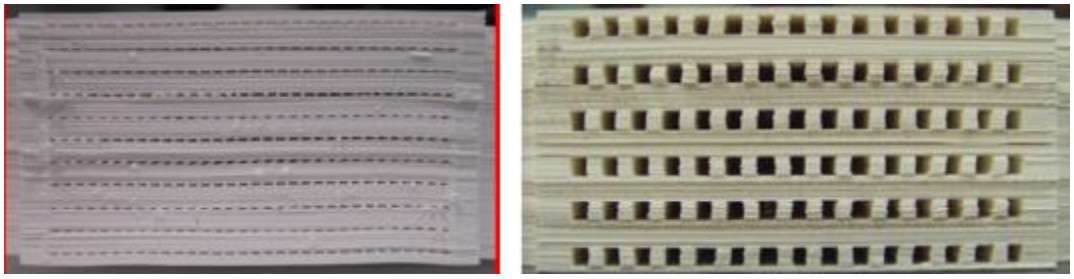

Design for Performance **Design for Build**

Figure 24: Comparison of DFP and DFB channel structure from side view. (Left) DFP prototype showing extremely fine channels, (Right) DFB prototype showing larger channels and fins.

The DFP model featured fine thin fins that required multiple internal supports, and a sacrificial external support to ensure fin alignment during the build. Two types of external fin supports were explored: 1) solid sacrificial strut and 2) ventilated sacrificial strut. Several experiments were performed to study the potential of removing the sacrificial struts while green. This would eliminate the necessity to machine the sacrificial struts off when fired, and allow air-flow to the internal channels during firing for better ventilation and even heat distribution. The green parts were found to be easy to cut with a ceramic blade, however strut removal caused compression of the channel openings and misalignment of the fins. This compression was much more pronounced for larger samples that require more manual force to cut through. The development of green machining DFP parts was beyond the scope of this project.

An important lesson learned from the green strut removal, which provided open channels, was that the quality of the fired sample greatly improved. The open channels allowed ventilation during firing, which eliminated bottom and side rupture cracks. This was shown to be especially true for larger samples. Ventilated sacrificial struts that could be removed after firing were then designed into the DFP. This design provided excellent build results, avoiding fin distortion from green handling, as well as outgassing flaws. The model was then built to full scale (Figure 19). The remaining corner cracks were eliminated with a final design modification that increased the corner fillet radius.

The DFB model was an outcome of lessons learned from the DFP design and build. DFB featured wider fins and channels, requiring fewer internal supports and no external supports due to the robust fins. This enabled successful full scale prototype builds within the scope of this program (Figure 24).

The DFP and DFB designs both have the same envelope but differ in the fin, channel, and separator plate dimensions. These differences are outlined below in Table 10. This setup allows for one rig to test multiple core designs by dropping them into a defined part envelope.

Table 10: DFP and DFB design comparison of fin and channel structure

	Design For Performance (DFP)		**Design For Build (DFB)**	
	Hot Side	*Cold Side*	*Hot Side*	*Cold Side*
Separator Plate Thickness	0.64 mm (4 layer)		0.32 mm (2 layer)	
Channel Width	0.69 mm	0.99 mm	1.50 mm	1.50 mm
Fin Height	0.80 mm (5 layer)	0.32 mm (2 layer)	1.90 mm (12 layer)	1.90 mm (12 layer)
Fin Width	0.41 mm	0.41 mm	1.00 mm	1.50 mm
Fin Aspect (h/w)	2/1	0.8/1	1.9/1	1.27
No. fins	39	31	20	17
No. internal struts	8	8	2	2

Two full-size DFB prototypes were fabricated. During the DFB-1 build, many techniques were refined layer by layer throughout the build. The lessons learned during the DFB-1 build were applied to the DFB-2 build and improved the overall part quality. The prototypes were machined and corner fillets smoothed for rig assembly (shown in Figure 25).

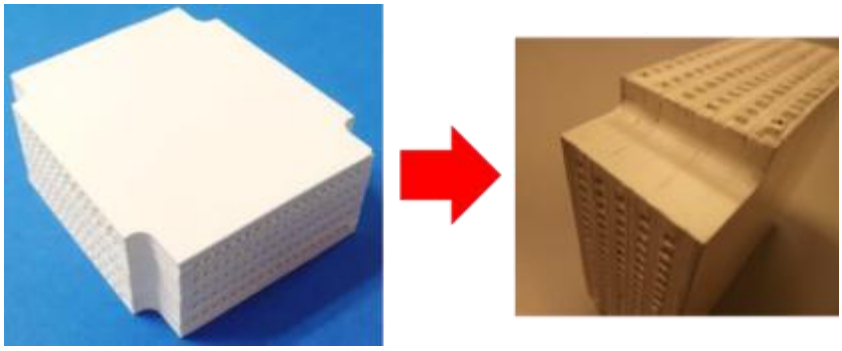

Figure 25: Full size Design for Build prototype shown before (left) and (right) after machining. Post-fabrication machining of the corner fillets enabled metal-ceramic seal necessary for testing.

Task 4 – System level challenges investigation

Experimental Methods

A method was developed to allow hermetic sealing without the need for a braze. The completed prototypes were machined on the sealing surfaces to a smooth finish (Figure 26). A graphite gasket was used to obtain a tight seal once the prototype was placed in the test rig.

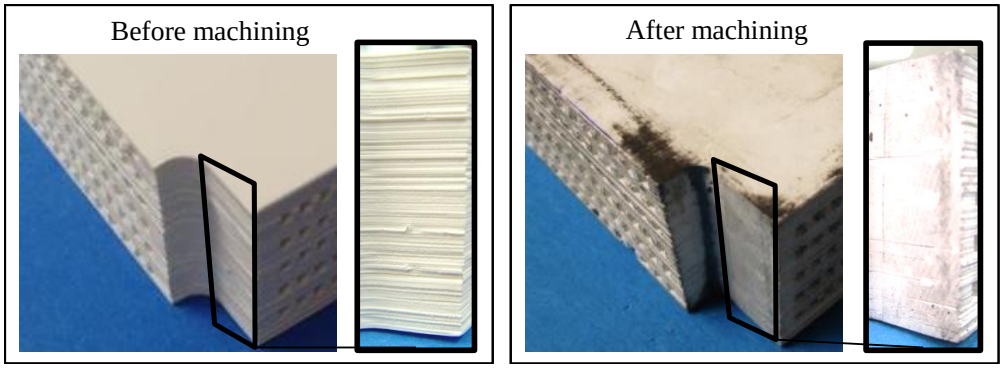

Figure 26: Prototype before and after machining. The "Before machining" corner view shows the rough finish from tape edges. The black residue in the "After machining" images is residual graphite from sealing into the rig.

Before beginning testing the part-to-rig seal was verified and the part checked for leakage between hot and cold channels. This test was performed by partially sealing the prototype into the rig, leaving the cold channels open (see Figure 27). The part-to-rig seal and internal part integrity were examined by creating a pressure differential between the closed channels and open channels, then examining the setup for leaks. The pressure differential was generated by drawing a vacuum on the sealed channels, and leaks located by a smoke test.

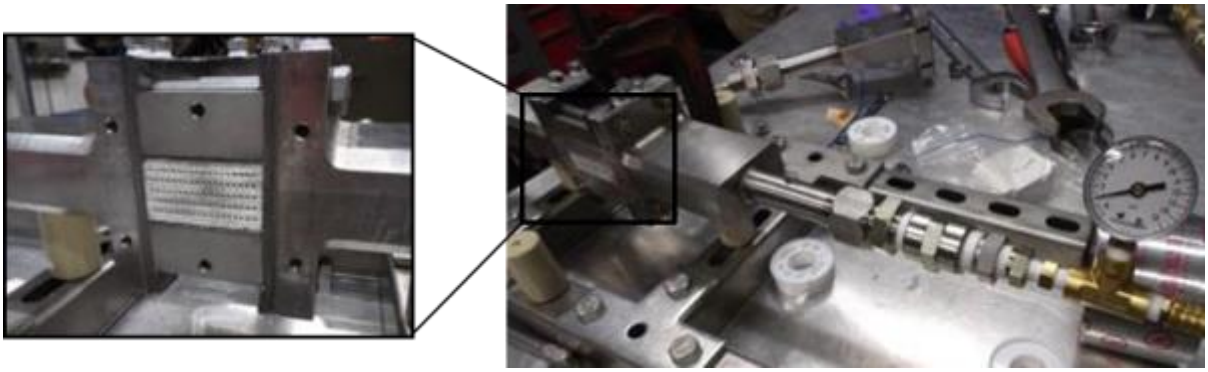

Figure 27: The partially assembled rig, set up for leak check testing. A vacuum is drawn on the hot channels. The open face of the prototype visible is the cold side, ready to be leak tested.

Another goal in this task was to perform a technology scale up analysis. The knowledge gained from prototype fabrication was used to envision a manufacturing process. This entailed setting reasonable parameters for the number of parts based on demand, material and labor costs, and process speed.

Results and Discussion

Task 4.1 – Seal heat exchangers for testing

The ceramic was able to be machined well, and resulted in smoothed corners, top and bottom surfaces (see Figure 26). Eliminating the manifold aspect of the design simplified the build and removed the stress failure-susceptible manifold bottom. The DFB-2 prototype was successfully sealed into the test rig using a grafoil gasket. The results of the smoke test showed that there was no leakage from the seal. However, leakage was detected between the hot and cold flow paths, as discussed in Task 5.

The sealing design eliminated the need for ceramic to metal brazing. It is possible for this mechanical fit design to be adapted to actual heat exchanger applications. The ZTM core can be functionally graded using two added tape compositions (discussed in Task 3.1, Figure 16), of zirconia/mullite, e.g. 50/50 and then 80% zirconia/20% mullite, to attach directly to zirconia tubes. The zirconia tubes have a good expansion match with Inconel and may be attached with a compression fit and grafoil gaskets instead of brazing. An important benefit of the design is that the core can easily be quality checked before distribution for use in the field.

Task 4.2 – Technology scale-up analysis

The knowledge gained from prototype fabrication was used to envision a manufacturing process. This was accomplished by setting reasonable parameters for the number of parts based on demand, material and labor costs, and process speed. The production scale-up investigation highlighted key areas for improvement after a close examination of the part build work-flow. The outcome of this study indicated that this method can be effectively scaled up for production. The complete report can be seen in Appendix B, and an overview can be seen below in Figure 28 with details in Figure 29, Figure 30, and Figure 31.

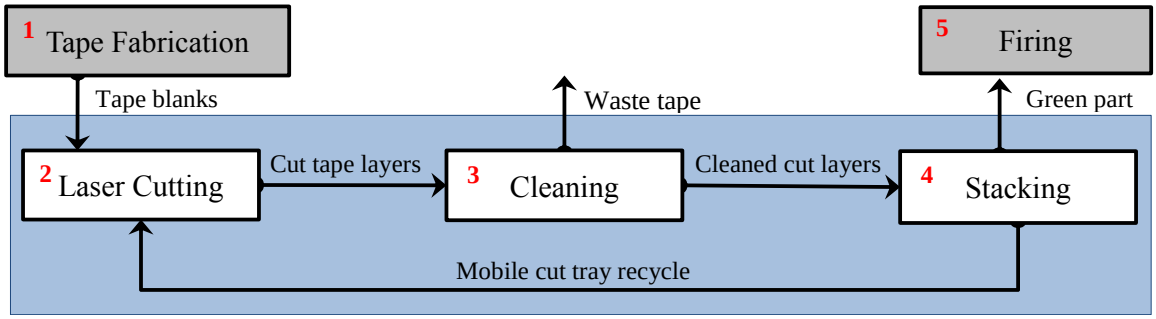

Figure 28: Commercial scale process diagram for laminated object manufacturing.

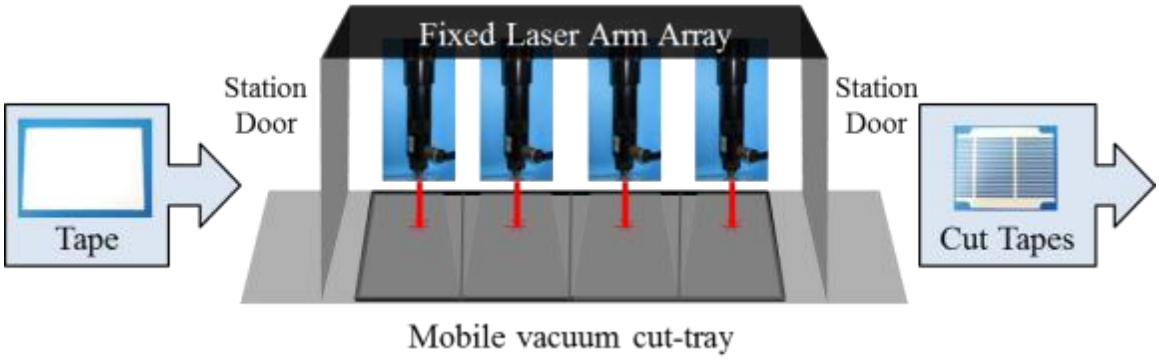

Figure 29: Laser cutting station. The station will consist of four lasers locked to the same mobile arm, encased in a UV protection coated plastic with sensor operated sliding doors. (**Step 2, from Figure 28**)

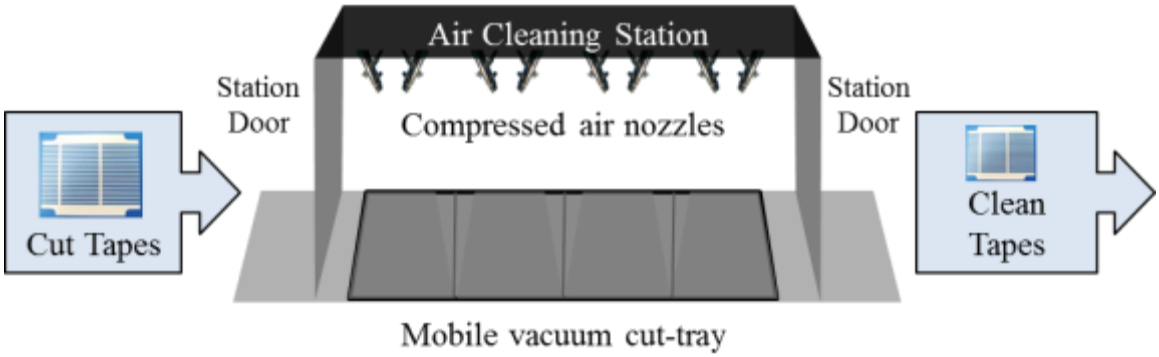

Figure 30: Cleaning station. The trays will lock in and engage the vacuum function to prevent dislodging during the air cleaning process. This consists of directed compressed air nozzles. (**Step 3, from Figure 28**).

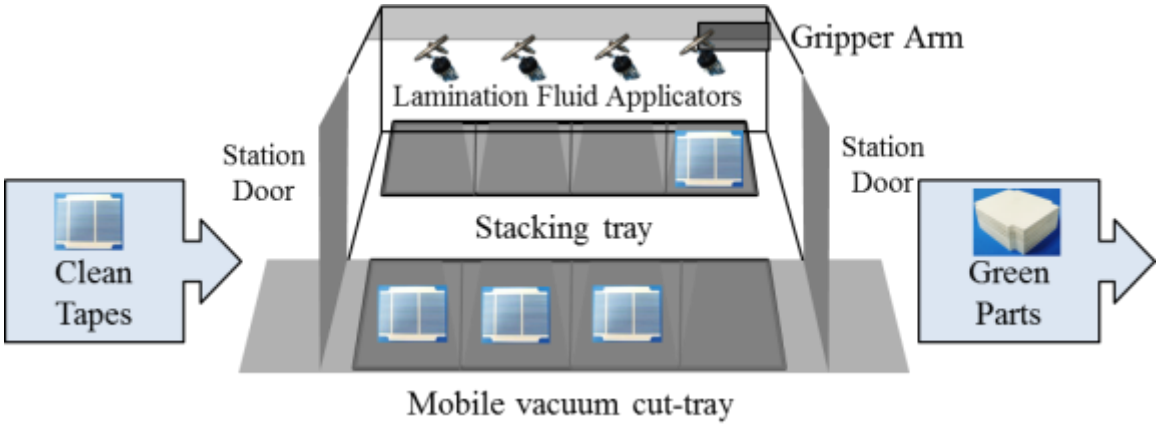

Figure 31: Stacking station. The tray will lock into place and use a gripper arm to pick up and stack each cut layer onto the stacking tray. Lamination fluid will be dispensed by applicator jets over each build slot. (**Step 4, from Figure 28**)

The scale up analysis focused on the production feasibility of 100 heat exchangers of 4 inch cube dimensions per month, based on the DFB design. The estimated cost to produce these parts is $1,200 per part (see Table 11). At this cost and a selling price of $4,000 per part, it appears that this approach is commercially viable.

Table 11: Prototype compared to projected production build costs

	2x2x1 in – Lab scale	4x4x4 in – Lab scale	4x4x4 in – 4 at a time production
Tape	$ 434 ($28/sq. ft.)	$ 4,838 ($28/sq. ft.)	$ 691 - $ 1,037 ($4 - $6/sq. ft.)
Labor	$ 875	$ 4,958	$ 159
Energy/part	$ 36	$ 9 (per part)	$ 5
Total	**$ 1,345**	**$ 9,805**	**$ 855 - $ 1,201 (per part)**

Opportunities to improve the production efficiency and reduce part costs were identified as 1) higher volume production, 2) increased laser speed, and 3) microwave assisted technology (MAT) firing. Conservative estimates were used for the costs of labor and tape, which may offer additional savings. The capital equipment costs are not considered in the analysis, however, all the machinery and components are commercially available technologies that can be customized for this system. The first system will require software development and engineering design, which can then be reproduced to increase capacity.

An additional improvement for mass production will entail the use of modular part building. Larger parts with over 200 tape layers have more opportunities for errors to cause expensive scrap. One or two fluid levels can be

achieved in a module of 30 tape layers. By building the parts from these modules, defective modules can be scrapped at lower cost.

The module design can be implemented at the separator layers. The first generation of full-sized heat exchangers would use the current cross-flow design shown in Figure 32. Looking forward to a second generation heat exchanger (Figure 33), the addition of a manifold structure would enable a counter-flow setup that has higher inherent efficiencies. Counter-flow heat exchange also reduces the thermal stress on the part. Both designs would incorporate the zirconia tube connector seal discussed previously.

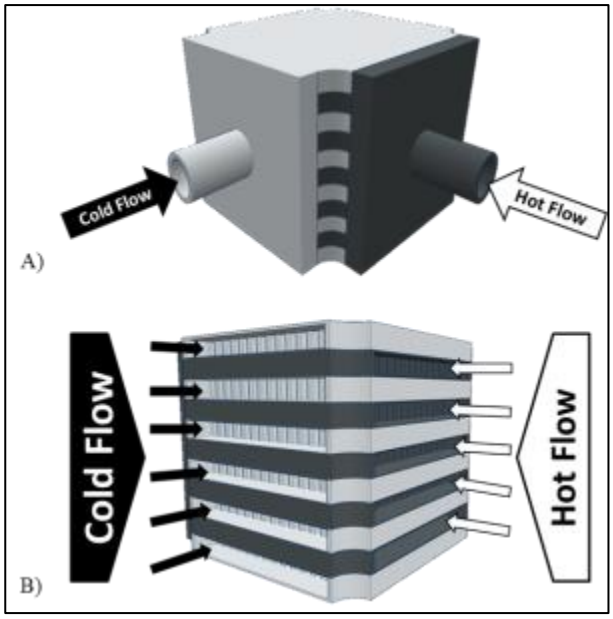

Figure 32: Model of a scaled up Generation 1 part using the same cross-flow heat exchange mechanism as the prototype fabricated and tested in this program. Hot flow layers: dark gray; cold flow layers: light gray. A representative number of hot and cold layers are depicted. A) External view of heat exchanger with simple manifold, showing how the hot and cold flows enter. B) Shows a view of the heat exchanger with the manifolds removed to show layer and channel structure. After entering through the manifold, the flow path continues into the channels of the multiple flow layers.

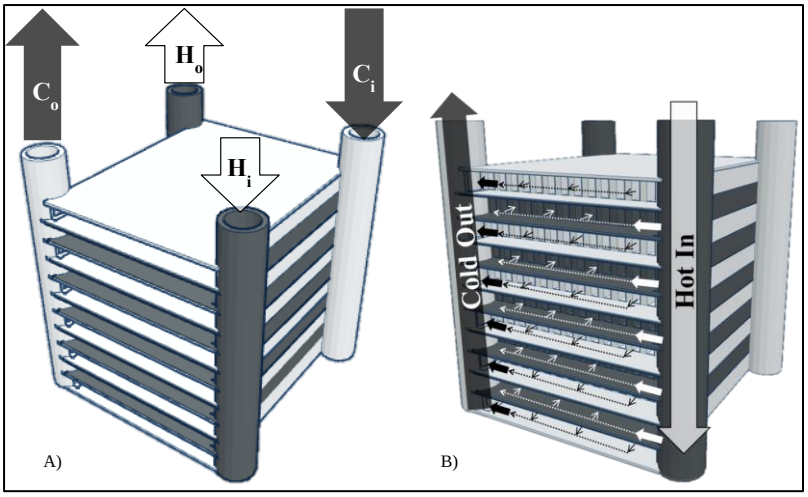

Figure 33: Model of Generation 2 part with counter-flow heat exchange. Hot flow layers: dark gray; cold flow layers: light gray. The counter-flow paths are indicated by the arrows represents the hot and cold flows passing in opposite directions. A) External view of the heat exchanger showing the hot and cold inlets and outlets (hot out: H_o, hot in: H_i, cold out C_o, cold in: C_i). B) Close view of the front facing side (A) showing direction of flow in hot and cold layers. Hot and cold flows enter through manifolds, and are distributed to each respective layer, bypassing the opposite layers.

Task 5 – Heat exchanger prototype performance testing

Experimental Methods

The following test methods were designed to demonstrate the capability of the ceramic heat exchanger to operate at high temperature. Performance, heat transferred and flow pressure drops, were measured. The ceramic heat exchanger was held in place by a set of hot headers, a set of cold headers and a set of U-shaped brackets (Figure 34). The headers are diffusers with a half angle of less than 7° to ensure uniform flow into the heat exchangers. Each header has a total of four instrumentation ports (two on top, and two on the bottom). Grafoil seals and rope seals are used to prevent leakage. Careful attention was given in making sure that enough compliance was provided by the Grafoil sealing elements so that the thermal growth of different components can be sufficiently accommodated.

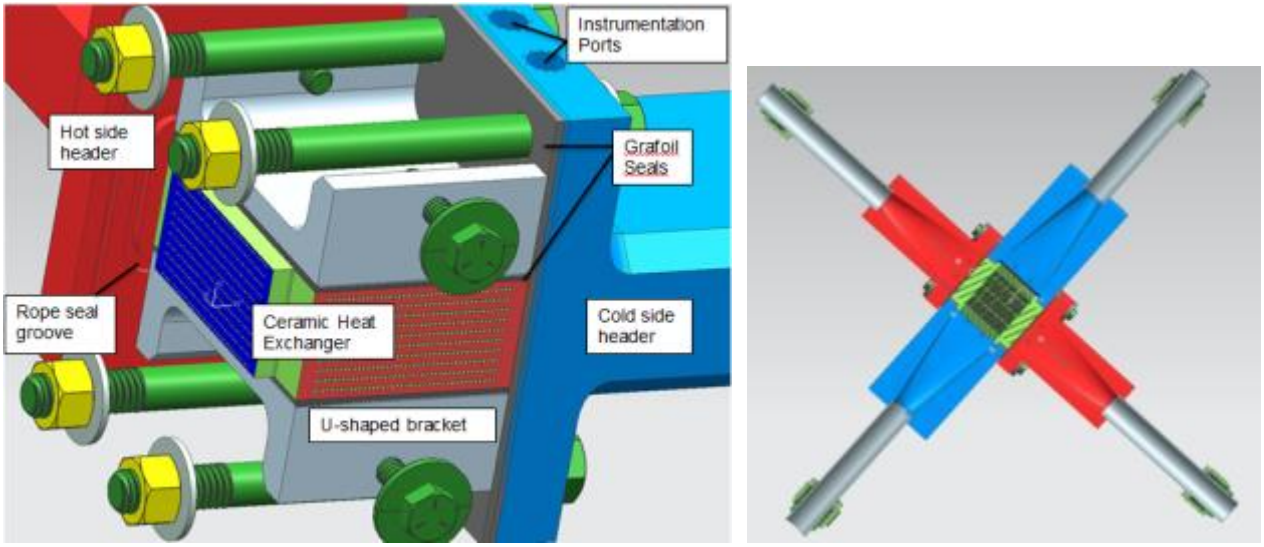

Figure 34: (Left) Partial view of the heat exchanger assembly. A hot side header and a cold side header are not shown. (Right) Cross section of the assembled heat exchanger.

First, the u-shaped brackets, the ceramic heat exchanger, and a set of grafoil seals were clamped together. Then the rope seal was installed into the hot side inlet and outlet headers. The headers were then attached to the u-bracket with bolts and Belleville washers. Finally, the cold side headers and additional grafoil seals were attached to the heat exchanger.

The experimental facility, known as the Jet Burner Test Stand (JBTS) is a self-contained combustion facility having eight test cells. The first five cells are designed for hot flow or combustion testing. The combustion test cells are each approximately 30x17x18 ft. with two test centerlines in each cell. Test cells six through eight are designed for cold flow testing (no combustion). A schematic of the test rig is shown in Figure 35. An electric heater was used to provide the cold air to the heat exchanger. An electric heater was also used during startup to heat up the hot flow. Both heaters were set to 401F during the start-up and heated the heat exchanger up to a constant temperature.

During testing, the electric heater in the hot stream was turned off and the hydrogen/air torch was turned on. The exhaust from the torch provided the hot flow into the heat exchanger. The temperature of the hot flow into the heat exchanger was controlled by the amount of hydrogen into the torch. The cold and the hot outlet flows are mixed downstream of the heat exchanger and then quenched with room temperature air.

Figure 36 shows the final test rig assembly for the 2x2x1 inch prototype. Two pressure measurements and two temperature measurements were taken at the inlet and the outlet of the cold and the hot streams. Mass flows were calculated with venturis upstream and downstream of the heat exchanger.

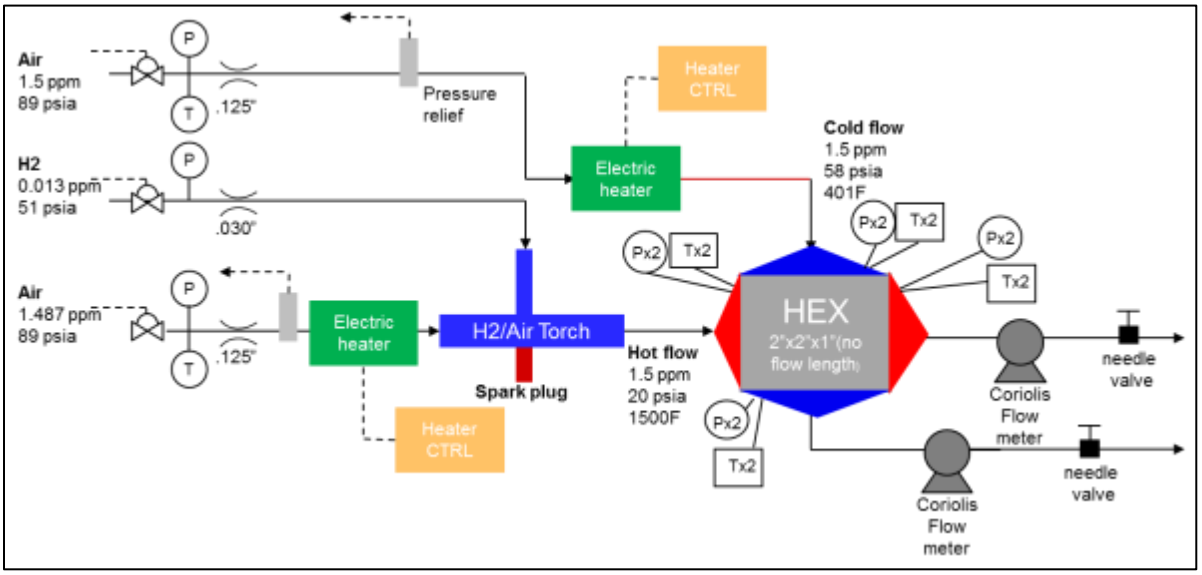

Figure 35: Schematic of test rig setup and control. The center of the rig is the fixture that holds and seals the heat exchanger prototype into place for performance testing. Both the hot and cold air flows are heated to simulate operating conditions, and to prevent thermally shocking the prototype. The temperature of the cold inlet is controlled by an electric heater to 400 °F. The temperature of the hot inlet is controlled by a hydrogen/air torch up to 1500 °F. Airflow is maintained through the heat exchanger by controlled pressurized air, 58 psia through the cold channels, and 20 psia through the hot channels. The exhaust hot and cold flow air is collected and quenched before exiting from the system.

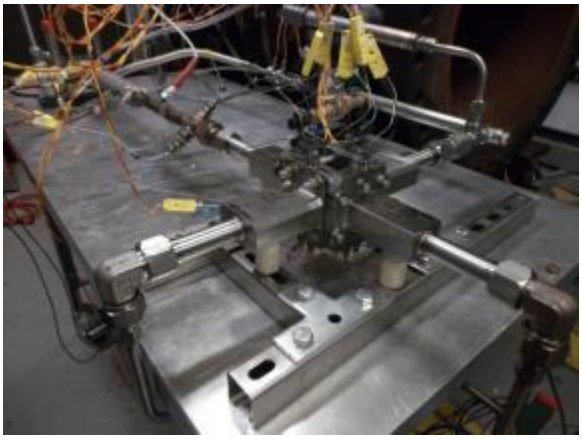

Figure 36: HX performance test rig with instrumentation

Micro computed tomography, a non-destructive 3D x-Ray technique, was performed using 225 KeV. A digital x-ray is performed by energizing photons through a source and capturing the results on a digital detector for viewing, after they pass through an object. Higher density objects are shown lighter and lower density objects are shown darker.

Results and Discussion

The DFB part, directly sealed into the rig, was tested for internal hot-to-cold cross-talk leaks. A leak was detected between several of the hot and cold channels on the top side of the prototype (see Figure 37). Minor cross-talk leaks may not be detrimental to the heat exchanger performance. Large cracks and areas of leakage will prevent the application of a pressure differential. In addition, cracks can grow under stress and thermal cycling, causing failure during testing or use. To better understand the internal structure of the ceramic prototype, the part was analyzed by micro computed tomography (micro CT) scanning. These results are discussed later in this section.

Figure 37: Shown is the leak checking process. The hot channels were sealed into the rig with a vacuum being drawn, and the cold channels were exposed. All but one row of the cold channels were masked by impermeable tape. As the vacuum was drawn on the hot channels, a smoke wand was passed over the exposed cold channels. The smoke is shown being drawn into the channels, indicating a leak between the hot channels and this row of cold channels.

For a test campaign for the high temperature conditions, different test matrices were developed summarized in Figure 38. Heat exchanger models were used to predict the heat transferred and pressure drops for the test conditions. The results are shown in Table 12 and Table 13. The predicted efficiency ranges from 0.33 to 0.39 as the hot inlet temperature increased from 600 °F to 1500 °F for Design for Performance, and 0.15 to 0.17 for Design for Build. These efficiency predictions are based on the 2 x 2 x 1" heat exchanger volume. The first target part for implementation is envisioned to have a volume of 4x4x4 inch with a corresponding efficiency of 0.60-0.65 for a high pressure drop and optimized fin design (Figure 2 Task 2.1).

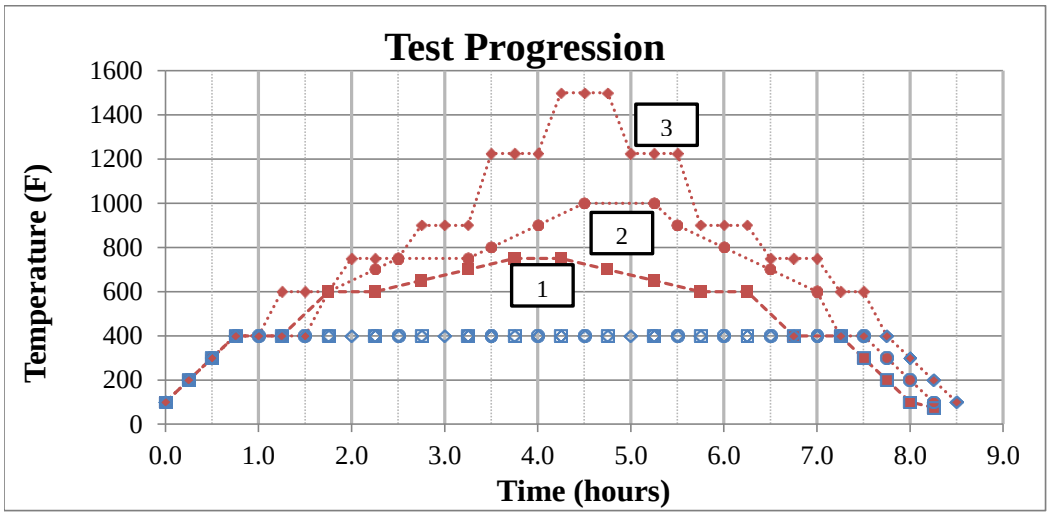

Figure 38: These heating schedules show the testing profiles for initial, intermediate and high temperature operation.

Table 12: Pretest predictions of outlet temperatures, heat transfer performance and pressure drops for DFP

Hot Side				Cold Side				Eff
Mass flow (ppm)	*Inlet (F)*	*Outlet (F)*	*dP (psi)*	*Mass flow (ppm)*	*Inlet (F)*	*Outlet (F)*	*dP (psi)*	
1.5	600*	535	0.79	1.5	401	467	1.19	0.33
1.5	750	634	0.93	1.5	401	520	1.26	0.34
1.5	1000	796	1.18	1.5	401	615	1.39	0.36
1.5	1250	954	1.45	1.5	401	717	1.53	0.37
1.5	1500	1110	1.75	1.5	401	825	1.68	0.39

*Torch ignition

Table 13: Pretest predictions of outlet temperatures, heat transfer performance and pressure drops for DFB

Hot Side				Cold Side				Eff
Mass flow (ppm)	*Inlet (F)*	*Outlet (F)*	*dP (psi)***	*Mass flow (ppm)*	*Inlet (F)*	*Outlet (F)*	*dP (psi)***	
1.5	600*	570	0.6	1.5	401	432	0.36	0.15
1.5	750	697	0.69	1.5	401	456	0.39	0.16
1.5	1000	908	0.87	1.5	401	499	0.39	0.16
1.5	1250	1118	1.05	1.5	401	544	0.42	0.17
1.5	1500	1329	1.23	1.5	401	592	0.42	0.17

*Torch ignition, **Corrected for tortuosity

The test rig was used to measure the performance of the DFB prototype. The performance data presented in Figure 39 shows the recorded hot and cold inlet and outlet temperature and pressure drops. The outlet conditions converged to a middle temperature, illustrating that heat exchange is taking place between the flows. Additionally, this shows that the hot side achieved a pressure drop of over 1.4 psi at the peak temperatures of 1300 °F. The cold side achieved a peak pressure drop of over 0.6 psi at the same temperature. The ceramic heat exchanger successfully withstood these temperatures and pressures without cracking or changing physical performance. Post-test prototype photographs are shown in Figure 40.

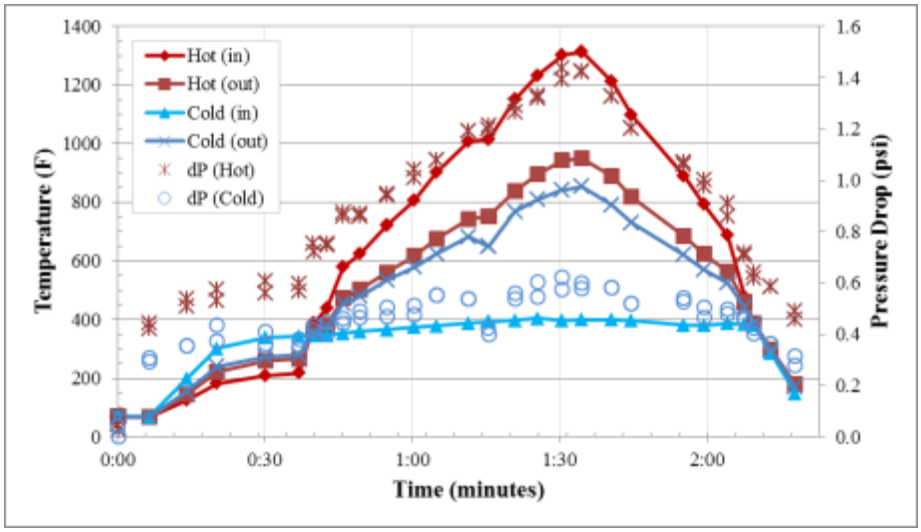

Figure 39: Performance data of DFB part. The ramp rate was implemented to prevent thermally shocking the part.

Figure 40: DFB prototype after testing showing the part handled the aggressive test conditions.

Efficiency was calculated from test results using the following formula where E is efficiency, T_{Co} is the cold outlet temperature, T_{Ci} is the cold outlet temperature, and T_{Hi} is the cold outlet temperature:

$$E = \frac{T_{C_o} - T_{C_i}}{T_{H_i} - T_{C_i}}$$

Specific points of interest between the predicted and actual performance results are presented below in Table 14. The results show the performance achieved by the DFB prototype exceeding the predicted efficiency by three times. This is due to prototype leakage from cold to hot side leading to flow mixing and an inflated heat transfer, artificially inflating the effectiveness. Model validation from measured effectiveness values cannot be derived; however, model calibration can be used to correct the pressure drop predictions in further design activity.

Table 14: Test results vs. model predictions for performance

Hot in (°F)	Cold in (°F)	Hot Side Pressure Drop (psi)		Cold Side Pressure Drop (psi)		Effectiveness	
		Predicted	Tested	Predicted	Tested	Predicted	Tested
578.5	353.5	0.6	0.87	0.36	0.44	0.15	0.45
722	366.5	0.69	0.95	0.39	0.5	0.16	0.47
1008.5	388	0.87	1.19	0.39	0.54	0.16	0.48
1233	405	1.05	1.32	0.42	0.61	0.17	0.49
1314	399	1.23	1.42	0.42	0.58	0.17	0.50

With the same inlet pressure levels (~48 psi) on both sides, cold to hot side mass flow leakage was noted to be <10%. With a given pressure differential between the two flow sides (8-10 psi), this leakage rate increased to ~23%. At higher inlet temperature on the hot side (1300 °F), a 5% leakage mass flow from cold to hot side was measured. This demonstrates the ability of operating this prototype at high temperature (>1300 F) as well as its ability to sustain higher temperature without growing defects/cracks which would have led to higher leakage rates. No catastrophic failure was noted during this high temperature test.

The DFB prototype was analyzed using micro computed tomography (micro CT scanning) to discover the source of cross talk. All of the compromising flaws occurred within a 2 mm zone that was 5 mm from the top of the 1 inch (25 mm) tall part, Figure 41. These flaws consist of cracks located in the separator plates between the top three rows of hot and cold fluid channels. The rest of the part did not contain any breaches that had an impact on the heat exchanger flow. This demonstrates that the building method was acceptable for the first 8 channels and suggests the use of a modular method, described in Section 4.2. As the part was built to a greater height, the previous part of the build was continuing to dry. This set up a stress in the junction between the separator plate and the fins. The bottom part was stiff, while the last few layers had a higher moisture level and were more flexible. Handling during this stage likely induced stresses that caused cracks to form during firing.

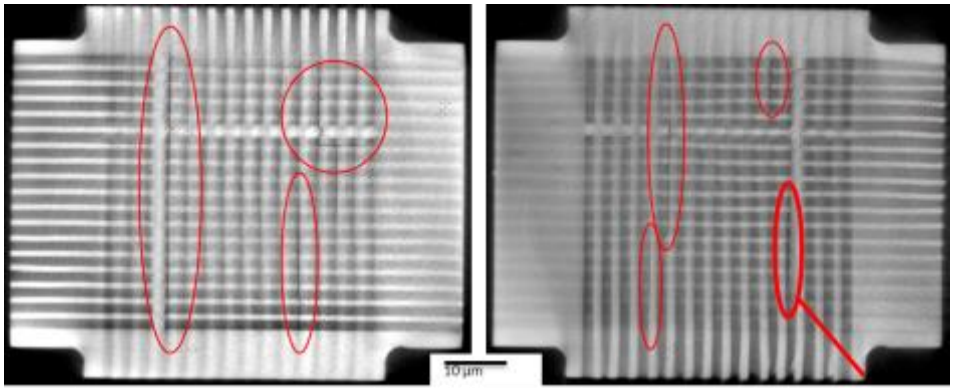

Figure 41: Pictured are two views of a micro CT scan focused on the flaw that caused the leakage during testing. (Left) 4.6 mm from top, (right) 2.5 mm from top

Further analysis showed minor cracks in the solid channel extension region designed to fit the heat exchanger into the rig, Figure 42. These cracks did not connect with the channels and therefore did not have an impact on the heat exchange flow paths. This demonstrates that the design, build, and ceramic material were fairly robust. Figure 44 shows typical cross sections, representing over 90% of the body of the prototype. The prototype had 8 of the 11 fluid layers intact. This clearly shows that a flaw free part can be built using the laminated object manufacturing method, with the limitation dependent on module height.

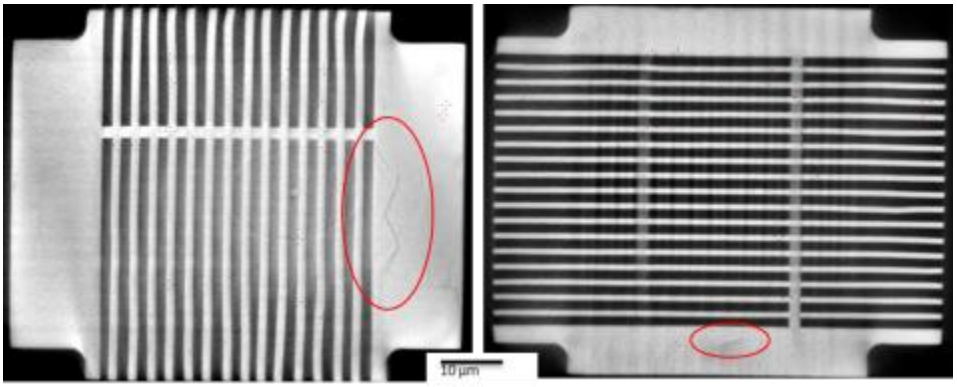

Figure 42: CT images of the DFB prototype (Left) shows the xy view 0.75 mm from the bottom surface of the part, (right) xy view of the prototype 3.5 mm from the part bottom. These small delamination cracks (circled) do not penetrate the channels.

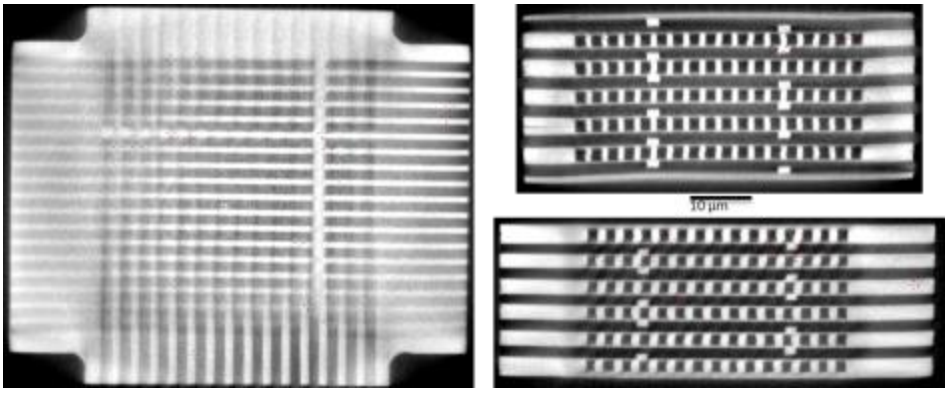

Figure 43: (Left) CT image cross section at a separator plate

Conclusions

It was demonstrated that complex ceramic heat exchangers can be built using laminated object manufacturing (LOM). The primary challenge was to develop a complete fabrication process that prevented defects in the ceramic. These defects were progressively eliminated through design and materials analysis. It was found that as the part height increased, the defect density increased. A height of 0.79" (20 mm) was built without significant flaws. Above this height, defects caused cross talk cracks that prevented a pressure differential greater than 10 psi during testing.

Modeling was used to understand the relationship between material properties, fin geometries, and the expected performance of the heat exchanger. At this stage of development, efficiency on the order of 0.2 can be achieved with the advancements made in LOM during this program. Higher efficiency, up to 0.65, will require further development in LOM processing to increase the speed and automation. Faster laser cutting, with better precision stacking software, and less green handling is essential for the fabrication of finer heat exchanger geometries.

A scale up analysis using the currently achievable design indicated that the ceramic heat exchanger could be manufactured at a reasonable cost. The envisioned manufacturing process would incorporate the following features:

- Automated tape feed and lamination fluid control
- Cutting speed increased by 5x with mobile laser
- Use of module with 6 fluid flow layers each for reduced risk of flaws
- Parallel module builds

The successes in this program have far reaching implications. Additive manufacturing of ceramics has lagged behind the development for metals and polymers due to the challenges of adding and densifying ceramics in layers. Laminated object manufacturing is one of the few techniques with promise for obtaining high resolution, high density ceramics. The method enables the fabrication of parts with fine internal channels and therefore is an excellent fit for ceramic heat exchangers. The lack of efficient manufacturing technologies has inhibited the development and application of these heat exchangers. These lighter, more efficient ceramic heat exchangers allow higher temperature operation, reducing CO_2 emissions and are in demand for microturbine power recuperation. Higher operating temperature is an essential next step to enable efficient power generation in the 21st century. Another example is the need for compact ceramic heat exchangers in Un-piloted Aerial Vehicles (UAV) which are increasingly used for military and disaster relief missions. The work performed in this program provides the groundwork for future development of ceramic additive manufacturing and complex ceramic heat exchangers.

References

1. Glymond, D., *Fracture toughness and creep of mullite and mullite based composites.* 2013.
2. Martin, R., et al., *Powder Injection Molding of Ceria-Stabilized, Zirconia-Toughened Mullite Parts for UAV Engine Components.* JOM Journal of the Minerals, Metals and Materials Society, 2013. **65**(11): p. 7.
3. Vick, M.J., *High efficiency recuperated ceramic gas turbine engines for small unmanned air vehicle propulsion.* 2012.

List of Acronyms and Abbreviations

LOM - laminated object manufacturing

DFP - design for performance

DFB - design for build

AlN - aluminum nitride

ZTM - zirconia toughened mullite

k - thermal conductivity

XRD - x-ray diffraction

ZrO_2 - zirconia

DFB-1 - design for build prototype, first prototype

DFB-2 - design for build prototype, second prototype

DFP-1 - design for performance prototype, first prototype

micro CT - micro computed tomography

JBTS - Jet Burner Test Stand

UAV - Unpiloted Aerial Vehicle

Project Manager - Jason Hissam
Department of Energy
National Energy Technology Laboratory

March 13, 2015

Appendix A

Characterization Report

Task 3.3
Milestone 3.3

Prepared By:
Nicole Ross
Dr. Holly Shulman

Ceralink, Inc. 105 Jordan Road Troy, New York 12180 518-283-7733

105 Jordan Road
Troy, NY, USA 12180
Phone (518) 283-7733

www.ceralink.com
info@ceralink.com
Fax (518) 283-9134

Summary

This report is to document the characterization work performed in Task 3.3. Delivery of this report completes Milestone 3.3. The goal in this task is to evaluate the new process that is being developed: using laminated object manufacturing to build ceramic heat exchangers.

In this task, key problems were identified and solved through process and design adjustments. The major challenges relate to joining of the ceramic tape layers and preventing distortion of the fine cut features.

It was found that lamination defects caused by macroporosity created strength limiting flaws. These major defects were eliminated by adjusting the heat treatment schedule to allow slower binder removal. Minor defects were caused by fine particle dust settling on the ceramic tape prior to lamination. This is being addressed with a cleaning procedure.

The heat exchanger design requires fine features which can become distorted when moved during the laminate stacking or firing. With feedback from Ceralink's fabrication and analysis, UTRC has provided a more robust design. This promotes handling and stacking stability. In addition, distortion was caused during firing shrinkage, which was solved by using a smooth surface to prevent shrinkage friction.

From this analysis there is a high degree of confidence that the ceramic heat exchanger prototype can be built effectively using laminated object manufacturing.

Shrinkage and Densification

Zirconia toughened mullite (ZTM) was selected for prototypes. X-Ray diffraction was used to verify that the ZTM composites would not form unwanted reaction phases. Three candidates for the source of mullite (Table 1) were considered based on cost, particle size, purity, and availability.

Table 1: Property summary of mullite sources.

	M1 mullite	M2 mullite	M3 mullite
Particle Size	44 um	1 – 5 um	0.7 um
Purity	Al_2O_3 75.0 % SiO_2 24.7 % Other 0.3 %	Al_2O_3 73.19 % SiO_2 25.65 % Other 1.16 %	Al_2O_3 71.9 % SiO_2 28.0 % Other 1.12 %
Tape quality	poor	good	excellent

Firing of representative ZTM composites at 1500 ^{o}C showed that M1 ZTM did not densify well, and was eliminated as a candidate. A firing test at 1550 ^{o}C (Table II) showed that M3 ZTM had the highest shrinkage and densification. Therefore, M3 ZTM was down selected for this project. The firing temperature was increased to 1570 ^{o}C for full densification of M3 ZTM.

Table II. Shrinkage and density of ZTM candidate composites

	Shrinkage	Theoretical Density
M2-ZTM 1550 ^{o}C	16.1%	93.3%
M3-ZTM 1550 ^{o}C	26.6%	97.6%
M3-ZTM 1570 ^{o}C	26.5%	100%

The linear shrinkage of 26.6% is a good match with zirconia at 26-28%. This is critical for co-firing in later stages.

The M3 ZTM consists of 80 vol% KCM101 mullite and 20 vol% 3YS Tosoh zirconia. Figure 1 shows an SEM micrograph taken from a laminated tape section fired at 1570 ^{o}C. The microstructure appears fully dense, uniform and well mixed.

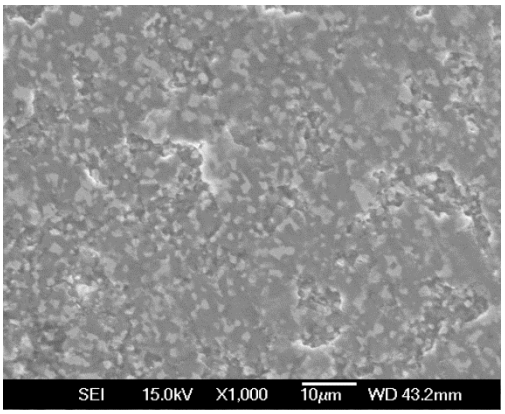

Figure 1. SEM micrograph of M3 Zirconia Toughened Mullite fired at 1570 ^{o}C showing uniform, well mixed microstructure. Light regions = zirconia, gray = mullite

Lamination

A proprietary lamination fluid is used to promote adherence of the ceramic tapes. A study was conducted comparing different lamination conditions including time, temperature, pressure, and quantity of lamination fluid. It was determined that the most significant factor for good adhesion of green tapes is the quantity of lamination fluid. With too much fluid, the tapes distorted, and with too little, tapes did not adhere. A formula for the ratio of lamination fluid to tape surface was developed. Figure 2 shows an example of distortion due to excessive lamination fluid.

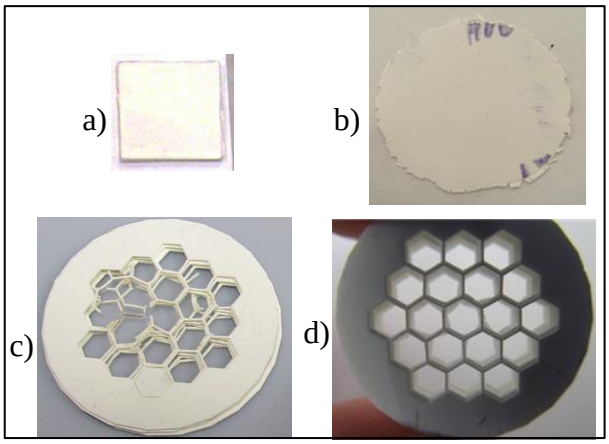

Figure 2. a) 1 x 1" square 6 layer laminate before pressing,
b) after pressing with distortion due to excessive lamination fluid,
c) 6 layer laminated honeycomb structure showing distortion from tape excessive lamination fluid causing tape softening,
d) 20 layer laminated honeycomb structure without lamination fluid distortion.

Lamination quality was determined by cross sectioning parts and observing with optical and SEM. Flaw types, sizes and shapes were catalogued and related to processing methodology. A system for quantifying laminated tape interfaces was developed. This consists of using a line intercept method to measure the delaminated regions and compare to the total linear lamination interface.

Figure 3 shows the cross section of a 20 layer laminated stack fired to 1570 C. A typical rate for binder removal, 1 ^{o}C/min produced a high degree of delamination (40%) (Fig 3a). When the heating rate was lowered to 0.3 ^{o}C/min the linear delamination decreased to less than 5% (Fig 3b).

a)

b)

Figure 3: M3-ZTM 20-layer laminated tape cross-section, binder burn out 600 ^{o}C, subsequently fired to 1570 ^{o}C. a) Burnout rate 1 ^{o}C/min. b) Burnout Rate 0.3 ^{o}C/min. Binder from tapes caused delamination defects when removed too quickly.

Once the binder related large flaws were eliminated by adjusting the binder burnout rate, the smaller delamination areas were studied in greater depth. Examination of the cross-section of the 20-layer tape sample (Fig. 3b) showed small delamination cracks between some of the tape layers. Optical and SEM observation show small particles evident in the openings of the delaminated areas, Figures 4a and 4b. This resulted in up to 5% linear delamination. The particles are most likely caused during laser cutting of the tape, by ejection of cutting debris onto the tape surface. Effective sintering of layers was inhibited in the immediate surrounding area by the dust particulate. These flaws will be addressed by implementing a cleaning procedure during prototype building.

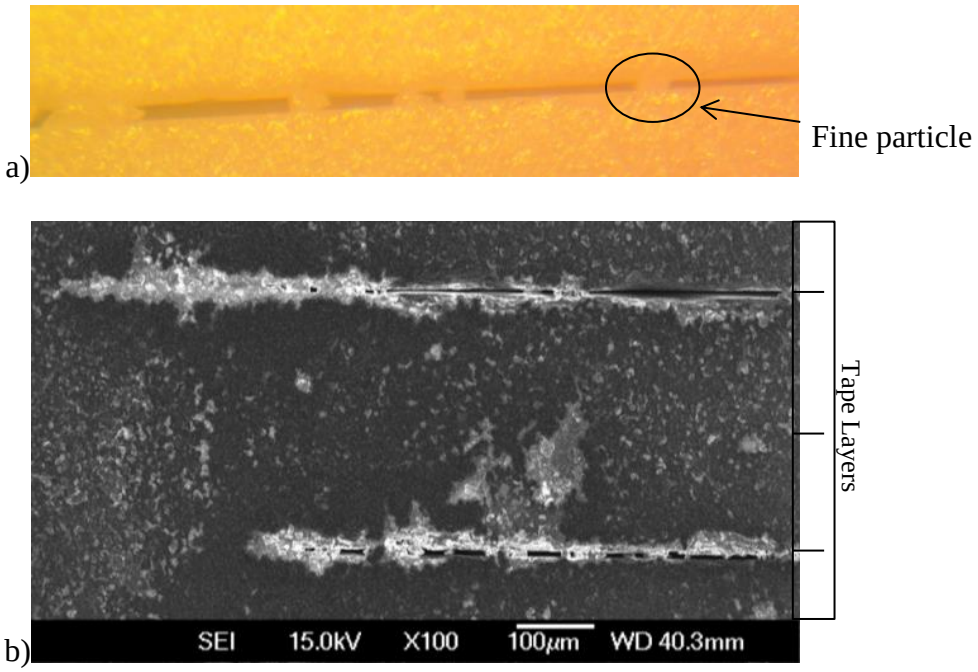

Figure 4. M3-ZTM 20-layer laminated tape cross-section micrographs showing delamination due to fine particulate fragments. a) Optical. b) SEM.

Figure 5 shows the typical cross-section of laminated ZTM tapes with the slow binder removal rate. Excellent bonding and uniform microstructure was achieved with the appropriate lamination fluid, pressing step, binder burnout rate, and firing temperature. Elimination of these flaws is critical to the overall strength of the ceramic heat exchanger.

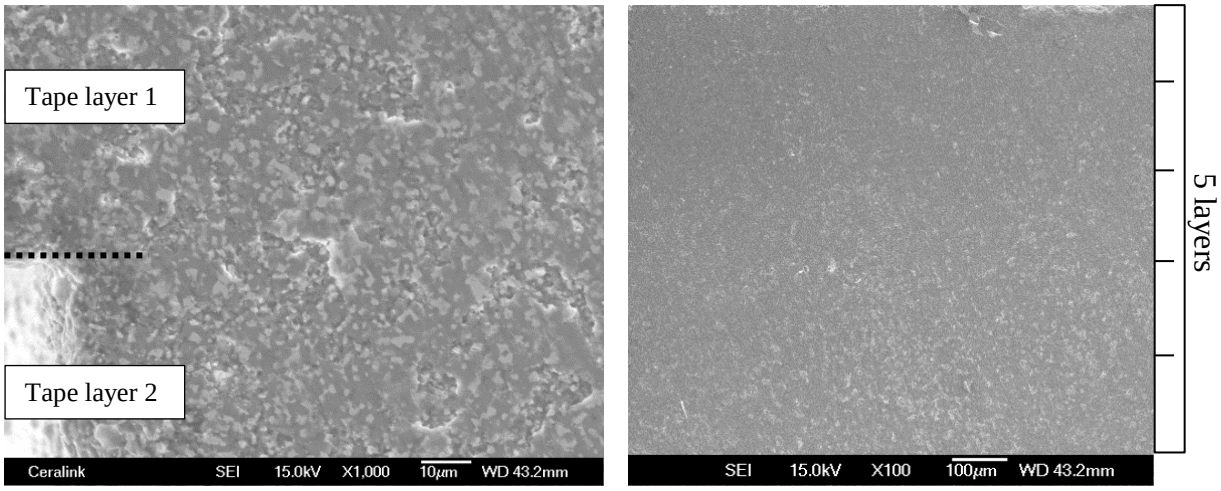

a) Two tape layers b) Five tape layers

Figure 5. SEM micrographs of M3-ZTM 20-layer laminated tape cross-section showing no differentiation between the layers indicating excellent bonding between ceramic tape layers.

Fine Feature Analysis

Laminated object manufacturing (LOM) is capable of producing fine features with a high degree of accuracy, however the desirable features push the limits of manufacturability. A simple robust design was constructed to explore the materials handling challenges. A nature inspired honeycomb structure with offset layers for airflow channels was built using LOM as pictured in Figure 6. The structure was fired successfully to high density. The building of this first prototype enabled a better understanding of the process parameters.

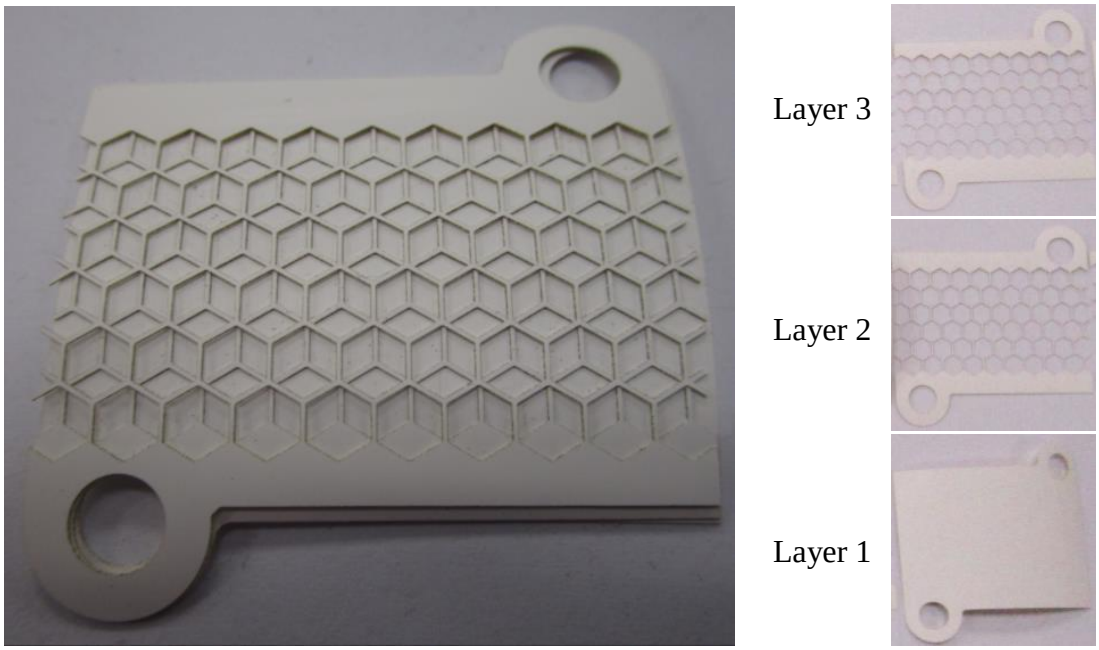

Figure 6: Manifold design, open flow pictured cut into green ceramic M3 ZTM tape. Design illustrates complex and precisely cut fine features with high connectivity lending stability to the individual layers. Layer 1) Solid layer separating open and closed flows. Layer 2) Honeycomb design. Layer 3) Offset honeycomb design.

The first model created by UTRC utilized a simple straight fin design with long cantilever fins connected only at one end. Figure 7 shows this design cut into green tape. The cut was aborted before completion due to the fins becoming misaligned and distorted during cutting. These defects were caused by the air pressure from the cutting laser which dislodged and moved the fins while the part was being cut. The part was able to cut well, but resulting part layer was not faithful to the original design due to the defects caused during the cut process.

a) b)

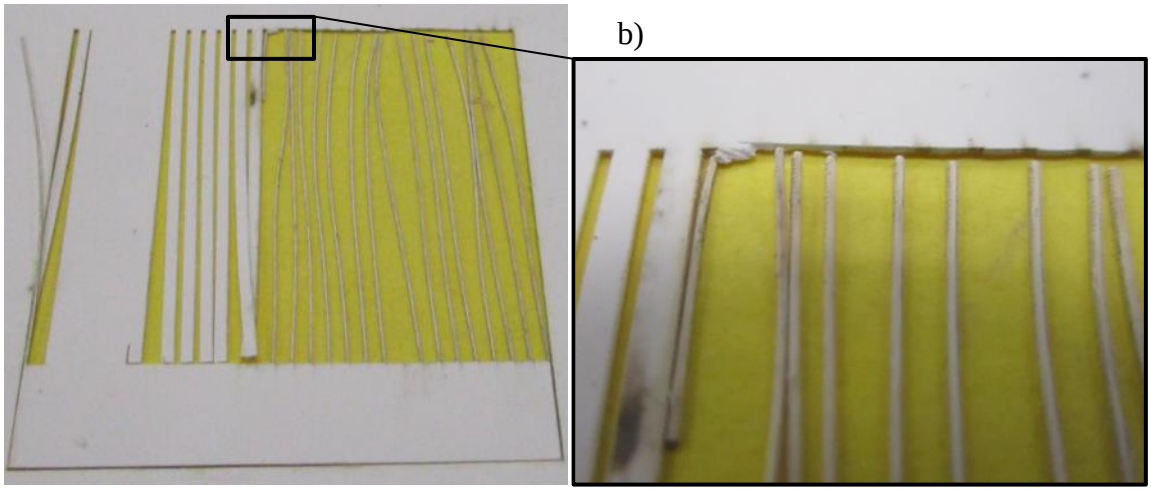

Figure 7. Cut green M3 ZTM ceramic tape in long cantilever fin pattern. a) Partially cut part. b) Close view showing distorted and misaligned ends fins. The distortion and misalignment are caused by air pressure turbulence during laser cutting.

To be able to effectively cut the part while maintaining fidelity to the design, a higher degree of connectivity was required between the fins. UTRC provided a modified design for testing with this adjustment. The design was converted to a contour file and cut in ZTM tape, as shown in Figure 8. It can be seen that the fins were accurately cut in the green tape without distortion.

During firing, several defects developed including minor distortion of fins, cracking off of orphan fins, and cracking off of an outer corner. These distortions and flaws are caused by drag of the fragile structure across a rough alumina setter during shrinkage. The high linear shrinkage (27%) and fragile structure requires special processing consideration. This is solved by the use of a smooth firing surface.

a) b)

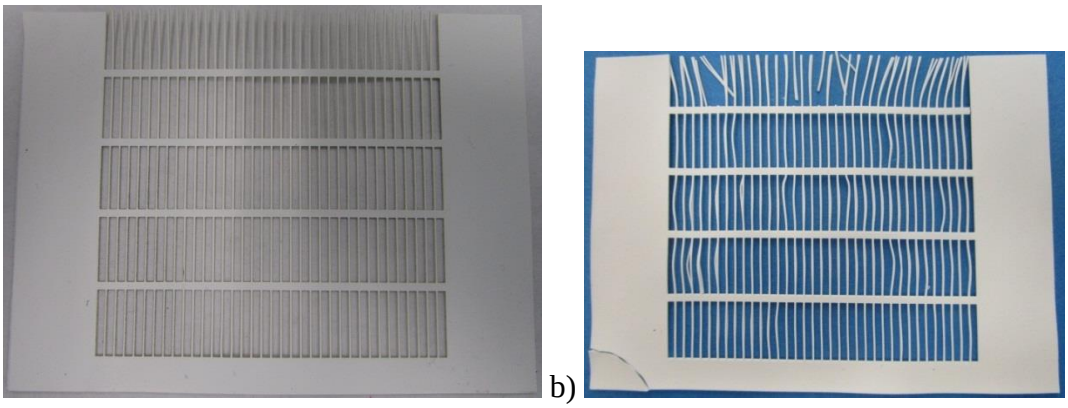

Figure 8. M3 ZTM 2-layer ceramic tape of open flow section from previous model iteration. a) Green cut tapes showing excellent cut that is accurate to the design. b) Fired part showing distortions in open fins, some internal fins, some broken orphan fins, and broken bottom right corner.

After identifying and addressing the challenges associated with lamination and distortion, UTRC has provided a more robust design for prototype building (Fig. 9). This design promotes handling and stacking stability to reduce the potential for distortion during the build process. This is accomplished by the addition of minor connections at the end of the unconnected fins. This connection obstructs and blocks the air flow, and will be removed after the part has been completely assembled.

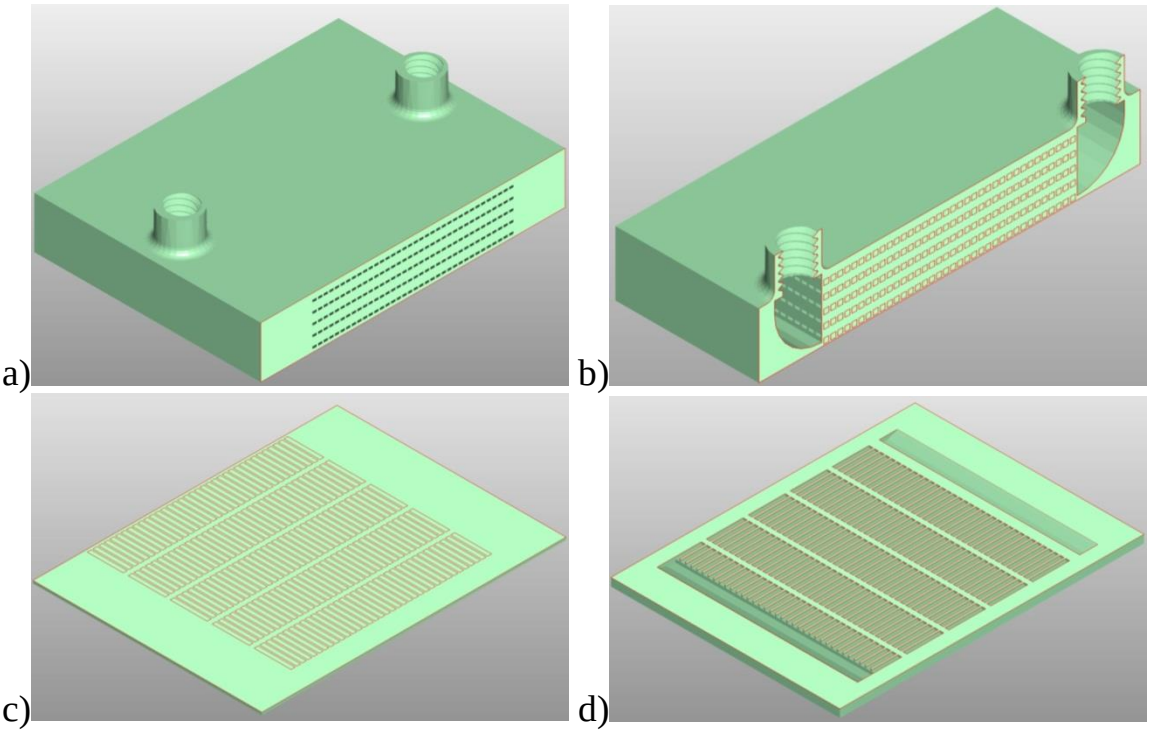

Figure 9. Robust manufacturable heat exchanger model with an open flow, and a manifold captured flow. a) External view of model, connection at the mouth of the open flow channels removed. b) Cross-section of model showing channel orientation. c) Open flow layer cross-section. d) Manifold captured layer cross-section.

The major processing challenges have been addressed through an iterative process of design modification and testing.

Conclusion

Key problems were identified and solved through process and design adjustments.

- Full density was achieved by choosing fine grain starting materials and adjusting the firing temperature.
- Tape distortion was remedied by control of lamination fluid during stacking.
- Macroporosity causing delamination was eliminated through decreasing the binder burnout rate.

- Micro-delamination caused by fine particulates is being addressed by implementation of a cleaning procedure prior to tape stacking.
- Distortion of fine features was caused by:
    1) Unsupported heat exchanger fins → mitigated by design optimization
    2) Transport of cut tapes → minimized by design and process improvements
    3) Friction of part during shrinkage → solved by use of smooth firing surface

This report concludes Milestone 3.3. This characterization task was used to understand and develop novel processing methods and designs that enable the fabrication of a complex ceramic heat exchanger. This work advances the understanding of ceramic additive manufacturing.

Project Manager - Jason Hissam
Department of Energy
National Energy Technology Laboratory

September 9, 2015

Appendix B

Next Generation and Scale-up Cost Benefit Analysis Report

Task 4.2
Milestone 4.2

Prepared By:
Nicole Ross
Dr. Holly Shulman

Ceralink, Inc. 105 Jordan Road Troy, New York 12180 518-283-7733

105 Jordan Road
Troy, NY, USA 12180
Phone (518) 283-7733

www.ceralink.com
info@ceralink.com
Fax (518) 283-9134

Contents

Summary

Laminated Object Manufacturing (LOM) is an additive process to build three dimensional parts from thin tapes. Current equipment has the capability to operate using a wide range of materials that can be made in to thin sheets or cast into tapes. This technology uses specialized software to translate computer models into two dimensional contours. These contours are precision cut with a CO_2 laser into the selected material tape, and precision stacked to build a part with internal features or channels.

The purpose of this report is to present an analysis of the commercial potential to use laminated object manufacturing for compact ceramic heat exchangers. From this study, there is a strong indication that the LOM method is commercially viable for this application. A scale-up scenario for production parts shows that market demand (cost and quantity) can be met using LOM.

Current Machine and Process Summary

The current prototype production is at a research laboratory scale, which includes a high degree of operator interaction. This process involves preparing each layer for laser cutting, cleaning, machine pick-up, lamination preparation, and stacking of the cut layers. Through repetition of these steps, green parts are built, then moved to a kiln for binder removal and sintering. The current process has two key areas for improvement:

- Excessive operator interaction, monitoring and inspection are costly and can introduce irregularities into the build.
- Single laser cutting is slow and non-optimized.

View of Commercial Process

Scaling up this technology to a commercial process will require new equipment design to provide a high degree of automation, with multiple lasers and high speed cutting. An overview of this process is presented below in Figure 1.

This new equipment will contain an array of lasers operating simultaneously. Each laser will cut five times the current speed through laser optimization. The higher degree of automation will allow for a more controlled, faster process with lower scrap rate. There are also significant opportunities for cost reduction in the feedstock tape and in the firing process. The process steps illustrated in Figure 1 will be discussed in more detail in the following sections.

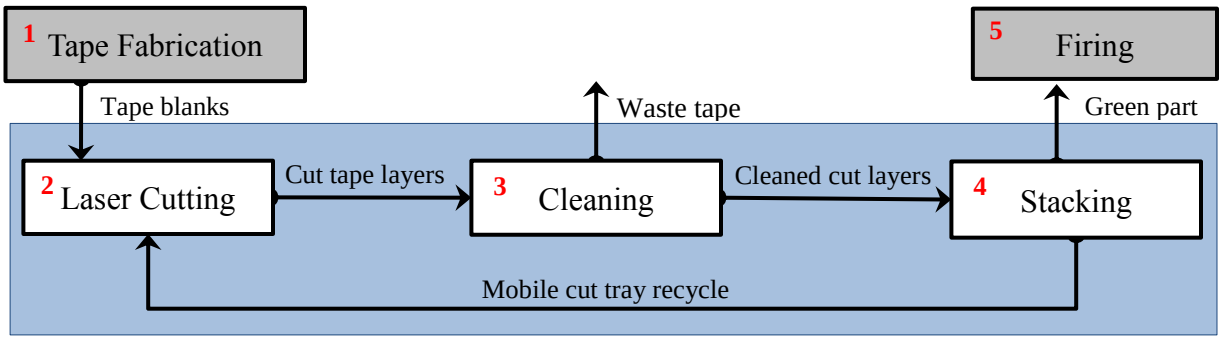

Figure 1: Commercial scale process diagram for laminated object manufacturing. The main LOM process is encompassed by the shaded box.

1 – Analysis of Current Prototype Cost

The information in this cost analysis is based on a 2x2x1 inch wide fin ZTM prototype (see Fig. 2) and applied to the desired commercial size of a 4 inch cube part.

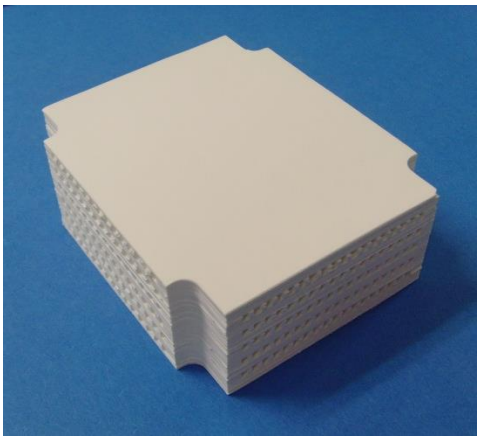

Prototype 2x2x1 Design: Wide fins and channels
- 1 mm cross section, 12 tape layer tall channels
- Alternating hot and cold flow layers
- Faces extended for direct sealing into test rig

Prototype 4x4x4 Design: Wide fins and channels
- 1 mm cross section, 12 tape layer tall channels
- Alternating hot and cold flow layers
- Manifold for brazing seal

Figure 2: Heat Exchanger via LOM Prototype fabricated for testing.

Tables 1 and 2 give a summary of the significant cost factors for the current process. The feedstock tape includes powders, non-aqueous binder and solvent. The laser time has an impact on the time to build the part, which affects the labor cost of the prototype. The labor rate for prototypes is based on an engineer level skillset. The primary energy cost is related to the ceramic firing process. Energy cost depends on the location and can range from $16 to $75 for one prototype part. There is an opportunity to drastically cut costs in all of these areas, as discussed in the following sections and Appendix A.

Table 1: Prototype build factors

	2x2x1 in	4x4x4 in
Tape	10” x 18.6 ft. (15.5 sq. ft.)	12” x 172.8 ft. (172.8 sq. ft.)
Labor*	30 hr	170 hr
Energy	1 prototype 1550 C 4 hrs	4 prototypes 1550 C 4 hrs

* Labor time includes machine setup, build preparation and troubleshooting time.

Table 2: Prototype build costs - detailed explanation and calculations are given in Appendix A

	2x2x1 in	4x4x4 in
Tape	$ 434 ($28/sq. ft.)	$ 4,838 ($28/sq. ft.)
Labor	$ 875	$ 4,958
Energy/part	$ 36 (1 part at a time)	$ 9 (4 parts at a time)
Total	**$ 1,345**	**$ 9,805**

2 – Cost Tolerance to Customer

Scale up operation is targeting 100 parts per month. A minimum of 10 parts per month and several sizes would be required by UTRCs parent company. Through an internal cost benefit analysis, UTRC has given a cost tolerance limit of $4,000 for the 4 inch cube ceramic heat exchanger. The cost estimate of $9,805 to produce the 4 inch cube prototype given the current laboratory scale method exceeds the cost tolerance limit. During the prototype fabrication process, key areas for cost reduction were identified.

3 – Cost Reduction Opportunities

Ceramic Tapes

Calculations show that 173 sq. ft. of tape is required for a 4 inch cube part (see Table 1 and Appendix A). Lab scale operations can produce tape for 2-4 parts per month, which is insufficient for the production volume (100 parts per month). Large scale ceramic tape production is well established, originally developed for electronics packaging. Commercial equipment is available for purchase or toll contracting.

Table 3 gives a breakdown of the materials and labor for laboratory scale ZTM tapes, showing that 75%-85% of the cost is in labor. The labor cost is drastically reduced in the industrial scale process. It is estimated that the cost of ZTM tapes can be reduced from $28 per sq. ft. to $4-$6 per sq. ft. based on saving in labor and economy of scale on materials purchasing. (See Appendix A)

Table 3: Costs based on current small scale production of tape

Cost Type	Cost per Square Foot	Cost Percentage
Tape (total)	$ 28	
Material	$ 4 - $ 7	15% - 25%
Labor	$ 24 - $ 21	85% - 75%

Fabrication

There is significant opportunity for cost reduction through automation and laser efficiency. Currently, engineering labor is required throughout the entire cutting process. The CAM-LEM equipment was originally designed and built in the 1990s for laboratory demonstration. It has since been upgraded; however, there are mechanical and software limitations that can be easily addressed with a modern design.

In the CAM-LEM, a single stationary laser cuts each layer by the precisely controlled movement of a mobile cut tray. The mechanical setup of this system currently limits the cutting speed to 17 mm/s. The high complexity of the cut pattern for each layer requires many rapid changes in direction of the cutting tray. This directional change, when operated at higher cutting speeds, causes a jerk reaction and leads to undesired differentiation of the corner contours. The cutting speed can be increased to 100 mm/s by 1) switching to a mobile laser and stationary cutting tray to reduce the mass of the moving part and 2) optimizing the laser focal length and power. Even with a technician continually stationed at the control console, the labor cost would be decreased by 87% per part, if 1 part is produced at a time (Appendix A).

The labor cost per part is further reduced by using an array of lasers to build multiple parts simultaneously.

The system can be fully automated from feeding tapes into the cutting zone, through cleaning and stacking as described in the following section.

4 – Scale up System

Commercial production will use ceramic tape as the feedstock. The tape will be spooled onto a roll that will load directly into the laminated object manufacturing (LOM) system. The LOM enclosed fabrication system will take the spool of cast tape and through the key process steps will fabricate green parts for firing.

Mobile Trays

The continuous LOM system will use a track with mobile vacuum cut-trays (see Fig. 3) that travel through the fabrication process steps and are recycled to the beginning. For the 4 inch cube parts, the cut-trays will be 24 inches long by 6 inches wide. This operational surface is to allow the parallel production of four parts at a time. The thin tapes will be held in place via vacuum suction similar to the current method. This feature is essential to prevent distortion of fine features during the cutting and cleaning processes.

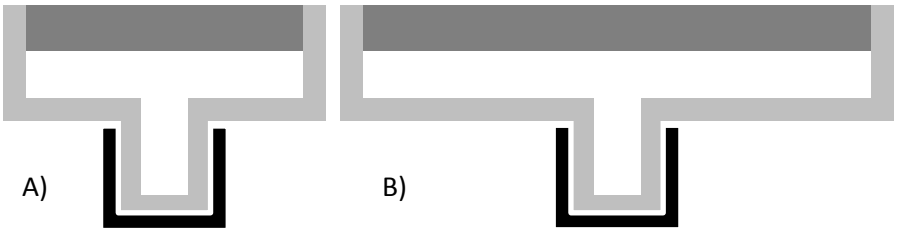

Figure 3: Cross-section of LOM system track and tray. A) Proposed 6" wide tray for 4 inch cube part. B) Alternate 11" wide tray for 8" part. **Light gray**: mobile vacuum tray casing, **White**: cut surface support and vacuum transfer area, **Dark gray**: cutting surface, and **Black:** the track.

After loading the spool of tape into the system, the mobile tray will pass under the tape-loading station. The tape will be automatically laid onto the surface of the mobile trays as they pass under the station, and held in place by use of the tray's vacuum function. As the tray passes from under the station, a blade will run across the back end of the mobile tray to sever the appropriate length of tape from the spool. The mobile tray will continue to the cutting station.

Cutting Station

The cutting station (see **Fig. 4**) will consist of four lasers that are locked to the same mobile arm, such that four parts will be cut simultaneously. The tray will lock into place for the duration of cutting. This is essential to prevent any small misalignments between the mobile tray and laser. The station will be encased in a UV protection coated plastic for operator safety and observation. Sliding doors will open and close to allow the mobile trays to enter and leave. The doors can be sensor operated, with the belt time controlled. This allows for the isolation of the steps, preventing cut tape debris and turbulent air currents from migrating to other stations.

A cutting speed of 100 mm/s can be obtained through system optimization based on the CAM-LEM design. (Note: the prototype used 17/mm/sec). This is a less efficient method than moving the laser to cut, due to the higher mass of the tray assembly causing a greater jerk reaction. By automating the laser arm to move instead, it is anticipated that cutting speeds greater than 100 mm/s will be achieved. For the purposes of this analysis, a conservative estimate of 100 mm/s will be applied. At this speed, the most complex layers of this design can be cut in less than 2.5 minutes.

Cleaning Station

The mobile trays with cut layers will travel from the laser cutting station to the cleaning station (see **Fig. 5**). The vacuum function will be engaged again to prevent dislodging during the air cleaning process. Compressed air streams will be directed at the cut tape layers for the removal of residual surface debris. The air-cleaning step will require a maximum of 5 seconds. After the cleaning, the mobile tray will be held in the cleaning station until the next tray is ready to enter. This station will also be isolated by sliding doors, and encased in a see-through plastic for observation. After leaving the cleaning station, the mobile tray will travel to the stacking station.

Stacking Station

The stacking station (see **Fig. 6**) will lock the mobile tray into place and use a gripper arm to individually pick up and precision stack each cut layer onto the corresponding build on the stacking tray. The parts will be built on the stacking tray, such that the mobile tray can be returned to the tape loading station.

The stacking or build tray will be a flat 24 in x 6 in aluminum tray for 4 side-by-side build operations. The system will be designed to accommodate different sizes. Lamination will be ensured by the weight or volume controlled dispensing of lamination fluid from an array of 4 fine-mist spray applicators over each of the build slots onto the top surface of each build-in-progress directly before its next layer is stacked.

The pick-up of each layer will be carefully controlled by the design of the gripper mask. This mask allows the gripper to pick up by vacuum suction the cut layer, leaving any waste tape (border material and removed cut sections) on the mobile tray. The stacking pressure applied by the gripper arm will be controlled to ensure adhesion of each layer while preventing trapped pockets of air, or compression of the part.

The stacking station will be isolated in the same manner as the other stations to prevent contamination by the other stations and the external environment, and to ensure the lamination fluid does not migrate to other stations. The entire 4 cut-layer pickup, lamination fluid spray, stack operation takes 20 seconds.

After the cleaned cut layers have been stacked in the stacking station, the mobile cut tray will recycle back to the tape-loading station. During the recycle, the surface of the mobile tray will be automatically cleared of any remaining waste tape by high-pressure air.

Mobile Tray Recycle

The mobile vacuum cut-trays will travel through these stations continuously during part fabrication, holding in the cleaning station and in a 'ready to be used' line after tray recycling.

Operational Time Flow

The rate limiting step of the process is the cutting time. Combining the tape loading time with the time it will take to move the tray to the laser cutting station and cut the tape, this maximum time is 3 minutes per layer based on 2.5 min maximum cutting time. As explained previously, this time can be reduced further with laser optimization.

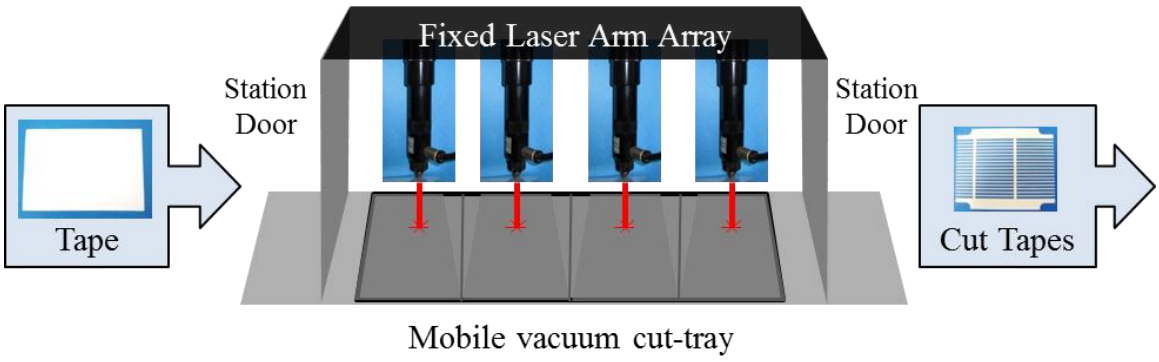

Figure 4: Laser cutting station. The station will consist of four lasers locked to the same mobile arm, encased in a UV protection coated plastic with sensor operated sliding doors. (**Step 2, from Fig. 1**)

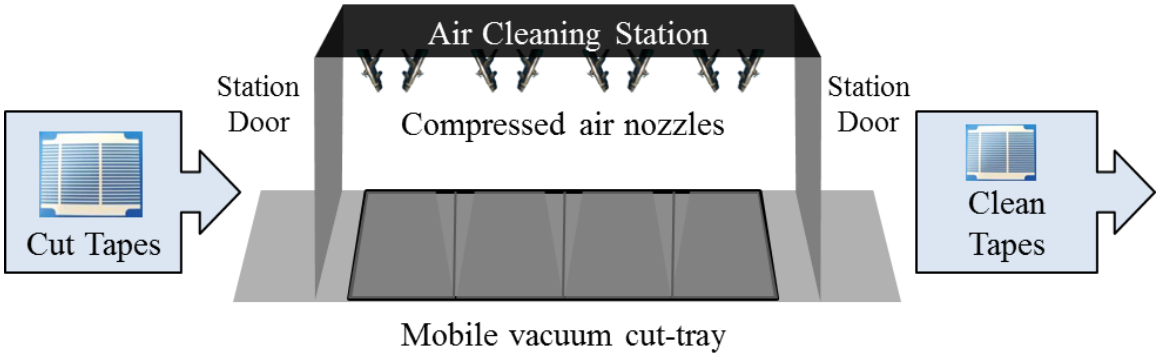

Figure 5: Cleaning station. The trays will lock in and engage the vacuum function to prevent dislodging during the air cleaning process. This consists of directed compressed air nozzles. (**Step 3, from Fig. 1**)

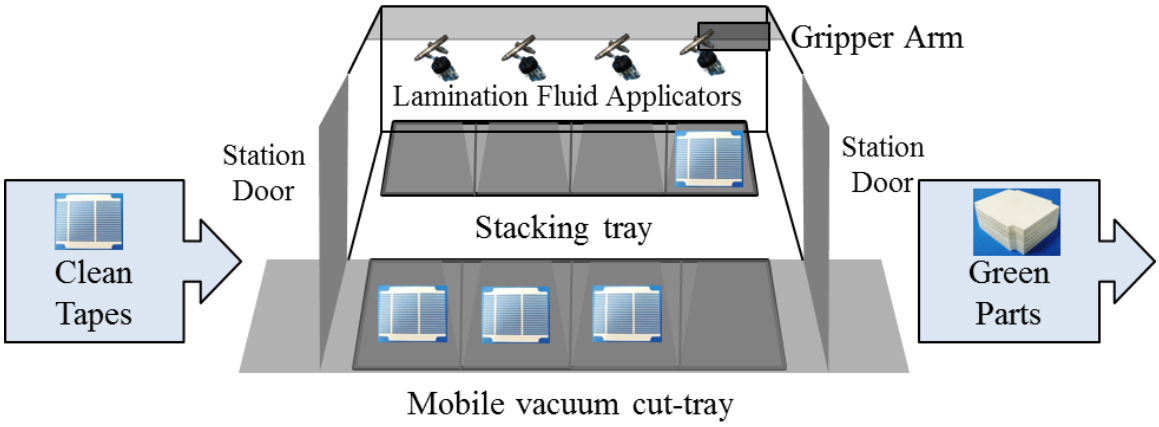

Figure 6: Stacking station. The tray will lock into place and use a gripper arm to pick up and stack each cut layer onto the stacking tray. Lamination fluid will be dispensed by applicator jets over each build slot. (**Step 4, from Fig. 1**)

Scale-Up System Summary

The LOM system will be enclosed from cutting to stacking in three stations. The rolled tape will be prepared in a separate operation and fed in and dispensed automatically before the first station. It is envisioned that the final firing step will be performed in a batch using Microwave Assist Technology (MAT) to enables fast firing. Ceramics fabricated from tapes contain a high volume of binders, which must be removed slowly during heating. MAT is a proven method to remove binders and fire at a faster rate by heating volumetrically.

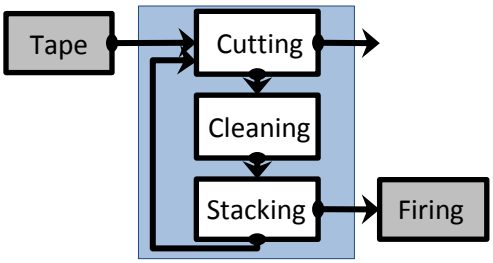

The conservative production settings will yield 4 parts per day. With a convention kiln, these require 3 days to fire. A fairly small (e.g. 4 ft^3) high temperature kiln is sufficient to keep up with the production of 4 part per day. It is anticipated that MAT will decrease the time to 1 day per firing, which will significantly decrease the work in process and operating cost.

Conclusion

The estimated cost to produce a minimum of 100 4 inch cube heat exchangers per month, based on the wide fin design (see Fig. 2) is $1,201 per part (see Table 4). At this cost and a selling price of $4,000 per part, it appears that this approach is commercially viable.

There are opportunities to decrease this cost further through 1) higher volume production, 2) increased laser speed, and 3) MAT firing. Conservative estimates were used for the costs of labor and tape, which may offer additional savings. The capital equipment costs are not considered in this analysis, however, all the machinery and components are commercially available technologies that can be customized for this system. The first system will require software development and engineering design, which can then be reproduced to increase capacity.

Table 4: Prototype compared to projected production build costs

	2x2x1 in – Lab scale	4x4x4 in – Lab scale	4x4x4 in – 4 at a time production
Tape	$ 434 ($28/sq. ft.)	$ 4,838 ($28/sq. ft.)	$ 691 - $ 1,037 ($4 - $6/sq. ft.)
Labor	$ 875	$ 4,958	$ 159
Energy/part	$ 36	$ 9 (per part)	$ 5
Total	**$ 1,345**	**$ 9,805**	**$ 855 - $ 1,201 (per part)**

Appendix A

Calculation of Lab-Scale Ceramic Tape Cost

The ceramic tape cost per square foot of $28 is found by examining the tapes used to build the 2x2x1 inch prototype. For this tape the following is given:

- Cost of tape: $3,900
- Length of tape: 170 feet
- Width of tape: 10 inches
- Tape total square feet: 141.7 square feet
- Cost of tape per square foot: $27.52
- Composition of tape by component mass

Material prices were investigated to yield the cost for each material, given the input mass. High and low estimates are $579 and #375 respectively for the tape.

From the calculated total cost per square foot, and the calculated material cost, a remaining cost can be found of $3,525 (low) - $3,321 (high). This remaining cost is labor.

The cost per square foot of the materials and labor break down as follows:

Table A1: (Expanded Table 3) - Costs based on current small scale production of tape

Cost Type	Total Cost per Tape	Cost per Sq. Ft.	Cost per Sq. Ft. in Table 3
Material	$ 375 - $ 579	$ 2.6 - $ 4.1	$ 4 - $ 7
Labor	$ 3,525 - $ 3,321	$ 24.9 - $ 23.4	$ 24 - $ 21
Total	$ 3,900	$ 27.5	$ 28

The values shown in Table 3 are more heavily weighted towards material cost to allow for price differences in the ceramic material.

Calculation of Lab-Scale Energy Cost

Temperature set-point, measured temperature and power output were measured for the firing of a full-sized prototype. The total power used was 220 kWh.

At a cost of 0.1544 $/kWh (varies by state http://www.eia.gov/electricity/state/), the total energy cost to fire sample 359 is $34 in NY.

Calculation of Scale-Up Ceramic Tape Cost

Commercial scale production of ceramic tape for this fabrication will be capable of producing a 20 inch wide tape at up to 20 in/min.

Assume high speed casting:

- 20 in tape cast at 20 in/min
- 2.8 sq. ft./min or 167 sq. ft./ hr tape produced
- Total of 3 labor hours per hour of casting time to incorporate the slurry and casting preparation time for a skilled technician labor rate

Labor cost = $0.13/sq. ft.

Assume slow speed casting:

- 20 in tape cast at 4 in/min
- 0.56 sq. ft./ min or 33 sq. ft./hr tape produced
- Total of 3 labor hours per hour of casting time to incorporate the slurry and casting preparation time for a skilled technician labor rate

Labor cost = $0.64/sq. ft.

Material cost for commercial scale production will be reduced due to economy of scale in material purchasing, making the maximum cost per square foot $4.

Table A2: Costs based on current small scale production of tape

Cost Type	**Cost per Sq. Ft. – Fast Casting**		
	Small Scale	Large Scale – Fast Casting	Large Scale – Slow Casting
Material	$ 4 - $ 7	$ 3 - $ 5	$ 3 - $ 5
Labor	$ 24 - $ 21	$ 0.13	$ 0.64
Tape (total)	$ 28	$ 3.13 - $5.13	$ 4.64 - $5.64

This cost is comparable to the industry production costs of $0.80/ft. (linear) or $1.33/sq. ft., which does not include estimated cost of the labor involved in slurry preparation or operation. This estimate validates the scale-up cost estimate for tape production as a conservative estimate.

Calculation of Scale-Up Total Cutting Time

Table A3: Total cut time per part for laboratory and automated build conditions

Design	2x2x1 in			4x4x4 in		
	Separator / Base	Vertical Channel	Horizontal Channel	Separator / Base	Vertical Channel	Horizontal Channel
No. Layers	30	72	60	94	264	252
Cut time per layer (s)*						
(Lab build)	24	166	232	48	664	928
(Automated speed 1)	7	47	66	14	188	263
(Automated speed 2)	4	28	40	8	113	158
Transition time						
(Lab build)	5 min/layer			5 min/layer		
(Automated speed 1)	15 s/layer			15 s/layer		
(Automated speed 2)	15 s/layer			15 s/layer		
Total time for single build (hr)						
(Lab build)	**21**			**166**		
(Automated speed 1)	**2.8**			**36**		
(Automated speed 2)	**1.9**			**22**		
Total time reduction for single build						
(Increase to speed 1)	**87%**			**78%**		
(Increase to speed 2)	**91%**			**87%**		

Cut times per layer for the 4 inch cube are based on scaling of measured cut times in the laboratory. The laboratory build speed is determined by the slow cutting speed of 17 mm/s and a long layer transition time of 5 minutes. At the production level that will be achieved by scaling up to an automated system, this transition time will be reduced to 15 seconds, and cutting speed increased 100 mm/s (speed 2). Speed 1 represents an intermediate speed (60 mm/s) that achievable for a stationary laser and XY moving cut-tray.

Calculation of Labor Cost Reduction by Scale-Up

Given the calculated total build time per part above in Table A4, the corresponding labor time can be determined. The true total build time (see Table 1) will be higher than shown above due to machine preparation and setup time, as well as troubleshooting time. This is especially true for the laboratory build times. Scale-up production will minimize the impact of these factors.

Building parts on the laboratory scale is time intensive and requires an engineer level skillset to accomplish. Building parts in the described scale-up production setting would be faster, and require monitoring by skilled technician. This translates to fewer less costly labor hours.

Table A4: Labor cost for 4 inch cube build

	Laboratory Build	Scale-up Production
Labor hours	170	30
Labor cost / build operation*	$4,958	$635
Labor cost / part	$4,958	$159

* Operation with four parallel part builds.

This represents a reduction in labor cost of 87% for a single build operation, and 97% per part.

Calculation of Cutting Tray Size

Shrinkage data for the large and full sized samples are shown in Table A6 below. All of the samples described were fired to 1550 °C for 4 hours.

Table A5: Shrinkage of full and large size samples

Sample No.	Shrinkage		
	X	Y	Z
353	25%	25%	24%
355*	25%	25%	25%
357*	25%	26%	21%
358	26%	26%	25%
359	25%	25%	25%
Average	25%	25%	24%

*Two step firing (bisque then full fire).

Shrinkage of the full scale parts is slightly lower than that of the smaller samples after arriving at the ideal firing profile for large parts. The footprint of green tape required for the parts active core are described in Table A7 below for three different sized parts: the current prototype (2x2x1 in), the scale up part (4 inch cube), and an even larger scale up part (8 inch cube). The green dimensions do not account for the necessary space a manifold would require, which is necessary for implementation.

Table A6: Footprint size of active core required for green tape.

Shrinkage	2x2x1 in (current)			4x4x4 in			8x8x8 in		
	X	Y	Z	X	Y	Z	X	Y	Z
25%	2.7 in	2.7 in	1.5 in	5.4 in	5.4 in	5.4 in	10.7 in	10.7 in	10.8 in
26%	2.8 in	2.8 in	1.5 in	5.5 in	5.5 in	5.4 in	10.9 in	10.9 in	10.8 in
27%	2.8 in	2.8 in	1.5 in	5.6 in	5.6 in	5.4 in	11.0 in	11.0 in	10.8 in

The 4 inch cube scale-up part being examined requires a 6x6 inch cutting space to account for the core and external manifolds.